Ultrastructural sublaminar-specific diversity of excitatory synaptic boutons in layer 1 of the adult human temporal lobe neocortex

Astrid Rollenhagen[1*], Akram Sadeghi[1*†], Bernd Walkenfort[2], Claus C. Hilgetag[3], Kurt Sätzler[4], Joachim HR Lübke[1,5,6]

[1]Institute of Neuroscience and Medicine INM-10, Research Centre Jülich GmbH, Leo-Brandt Str., 52425 Jülich, Germany; [2]Medical Research Centre, IMCES Electron Microscopy Unit (EMU), University Hospital Essen, Hufelandstr.11, 45122 Essen, Germany; [3]University Hospital Hamburg-Eppendorf, Center for Experimental Medicine, Institute for Computational Neuroscience, Martinistraße 52, 20246 Hamburg, Germany, [4]School of Biomedical Sciences, University of Ulster, Cromore Rd., BT52 1SA, Londonderry, UK; [5]Department of Psychiatry, Psychotherapy and Psychosomatics, Medical Faculty/RWTH University Hospital Aachen, Pauwelsstr. 30, 52074 Aachen, Germany; [6]JARA Translational Brain Medicine, Germany

*both authors have equally contributed to the study

†**Present address:** Research Group Anatomy, School for Medicine and Health Science, Carl von Ossietzky Universität Oldenburg, Ammerländer Heerstraße 114-118, 26129 Oldenburg, Germany

Address correspondence to: Joachim Lübke
Institute of Neuroscience and Medicine INM-10
Research Centre Jülich GmbH
52425 Jülich
Phone: +49-2461-612288
Fax: +49-2461-611778
E-mail: j.luebke@fz-juelich.de
Orchid ID: https://orcid.org/0000-0002-4086-3199

Abstract

Layer (L)1, beside receiving massive cortico-cortical, commissural and associational projections, is the termination zone of tufted dendrites of pyramidal neurons and the area of Ca^{2+} spike initiation. However, its synaptic organization in humans is not known. Quantitative 3D-models of excitatory synaptic boutons (SBs) in layer 1 of the human temporal lobe neocortex were generated from neocortical biopsy tissue using transmission electron microscopy, 3D-volume reconstructions and TEM tomography. Particularly, the size of active zones (AZs) and the readily releasable, recycling and resting pool of synaptic vesicles (SVs) were quantified.

The majority of excitatory SBs contained numerous mitochondria comprising ~7% of the total volume, had a large macular, non-perforated AZ (~0.20 μm^2) and were predominantly located on dendritic spines. Excitatory SBs had a total pool of ~3500 SVs, a relatively large readily releasable (~4 SVs), recycling (~470 SVs) and resting (~2900 SVs) pool. Astrocytic coverage of excitatory SBs suggests both synaptic cross talk or removal of spilled glutamate by astrocytic processes at synaptic complexes.

The structural composition of SBs in L1 may underlie the function of L1 networks that mediate, integrate and synchronize contextual and cross-modal information, enabling flexible and state-dependent processing of feedforward sensory inputs from other layers of the cortical column.

Key words: human neocortex, layer 1, synaptic complexes, quantitative 3D-models of excitatory synaptic boutons, astrocytic coverage, electron microscopy, TEM tomography.

Introduction

The mammalian neocortex is the most complex part of the brain comprising over 75% of the gray matter. One fundamental feature established during development is the formation of distinct layers with different networks of neurons, and its organization into vertically oriented slabs, so-called cortical columns (Marin-Padilla 1978, 1998; reviewed by Rockland and DeFelipe 2018). This organization is established in an 'inside layers first-outside layers last' fashion (Luskin and Shatz 1985a, b; reviewed by Cooper et al. 2008). The exception, beside layer (L)6 is L1 generated first originating from the marginal zone (Marin Padilla 1998; reviewed by Bystron et al. 2008). Ongoing cortico- and synaptogenesis finally lead to the formation of the adult cortical network with its unique structural and functional properties (reviewed by Lübke and Feldmeyer 2007; Rockland and DeFelipe 2018).

Remarkably, L1 is highly conserved across cortical areas and higher mammalian species, but its importance was long underestimated. However, L1 is now considered as the predominant input layer for top-down information, relayed by a rich, dense network of cortico-cortical, cortico-thalamic, commissural and associational long-range axonal projections. In humans, and thus different to experimental animals, both L1 excitatory Cajal-Retzius (CR) cells (Anstötz et al. 2014) and a quite heterogeneous population of inhibitory neurons (see for example Jiang et al. 2013; Boldog et al. 2018; Obermayer et al. 2018; Kwon et al. 2019; reviewed by Huang et al. 2024) provide signals to the terminal tuft dendrites of pyramidal neurons of the underlying cortical layers. Thus, L1 is a central locus of neocortical associations controlled by distinct types of inhibition and feedforward excitation (Schumann et al. 2019; Hartung and Letzkus 2021, reviewed by Schumann et al. 2021).

The temporal lobe neocortex (TLN) is situated on the basolateral aspect of the cerebral hemispheres primarily observed in higher primates, including humans. Notably, in humans, the TLN encompasses approximately 20% of the entire cerebral cortex (Kiernan 2012). It is recognized as a highly specialized associative neocortex, characterized by its homotypic granular six-layered organization (von Economo and Koskinas 1925; Palomero-Gallagher and Zilles 2019). The human TLN plays a crucial role in various cognitive functions, including auditory, visual, vestibular, linguistic, and olfactory processing.

Additionally, it is intricately connected to diverse sensory and multimodal associational brain regions, such as the limbic system, amygdala, and various subcortical structures (Insausti 2013). Lastly, the human TLN serves as the epicenter and onset site for temporal lobe epilepsy (Allone et al. 2017; Tai et al. 2018).

One of the most important discoveries in neuroscience, beside the definition of the neuron by Cajal's neuronal doctrine (1911), was the introduction of the term 'Synapse', more than 100 years ago. Since then these structures have been investigated from different viewpoints including structural, functional, molecular and computational studies summarized in meanwhile thousands of original publications, reviews and numerous textbooks. Yet, the quantitative geometry of the most prevalent synapse in the brain, the cortical synapse, has remained largely unexplored structurally, in both experimental animals (but see Rollenhagen et al. 2015, 2018; Bopp et al. 2017; Hsu et al. 2017; Prume et al. 2020) and, even more so, in the context of the human brain (but see Yakoubi et al. 2019a, b; Dominguez-Alvaro et al. 2019, 2021; Cano-Astorga et al. 2021, 2023; Schmuhl-Giesen et al. 2022; Shapson-Coe et al. 2024). This could be partially attributed to the availability of human brain tissue samples. Nevertheless, detailed and quantitative descriptions of synaptic complexes in L1 of the human brain are to date non-existing.

Here, an investigation into the synaptic organization of L1 in the human TLN was undertaken using high-resolution transmission electron microscopy (TEM), 3D-volume reconstruction, to generate quantitative 3D-models of synaptic boutons (SBs), and TEM tomography. The ultimate objective of this comprehensive project is to elucidate the synaptic organization, layer by layer, of the cortical column in humans.

Such meticulous quantitative structural analyses of SBs and their corresponding target structures are indispensable for comprehending, elucidating, and establishing connections between the structural and functional properties of the diverse signal cascades underlying synaptic transmission, efficacy, strength, and plasticity. Consequently, these efforts contribute significantly to the understanding of the computational properties of brain networks, in particular the synaptic organization of the cortical column.

Results

Neural and synaptic composition of L1 in the human TLN

L1 in the adult mammalian neocortex represents a relatively cell sparse layer, that in humans can be subdivided into two sublaminae, L1a and L1b, as revealed in semithin sections (Figure 1A) and Golgi-preparations (Figure 1B, C, F, G), as well as at the EM level (Figure 1H, I). L1a is more dominated by a dense network of astrocytes of different shape and size, their fine processes (Figure 2A), the occurrence of reactive microglia (Figures 1H, I, 2A) and terminal tuft dendrites of pyramidal neurons throughout the neuropil of L1 (Figures 1H, I, 2B).

Hence, L1a can be described as a sublamina with a predominant proportion of astrocytes, microglia and their processes, although it also harbors numerous other structural elements such as terminal tuft dendrites and synaptic complexes. These complexes consist of a SB juxtaposed with either a dendritic shaft or spine (Figure 2A) directly beneath or interwoven among the fine astrocytic processes within L1 (Figure 2A). Lipofuscin granules, indicative of aging, were frequently noted in astrocytes, reactive microglia (Figure 2A) and L1 neurons, although their abundance, size, and morphology varied considerably.

Remarkably, and in contrast to rodents, a persistent subpopulation of excitatory CR-cells was found in humans, identifiable by the horizontal bipolar orientation with intralaminar long-range horizontal axonal collaterals with a transcolumnar projection (Figure 1E-H; Retzius 1893, 1894; Anstötz et al. 2014; reviewed by Martinez-Cerdeno and Noctor 2014). The majority were located directly underneath the pial surface (Figure 1F, G) or intermingled with a heterogeneous population of GABAergic interneurons (Figure 1E).

In the human TLN, GABAergic interneurons constitute the predominant class of neurons in L1, exhibiting significant structural and functional heterogeneity (Figure 1D, E; see also Jiang et al, 2013, Verhoog et al. 2016; Boldog et al. 2018; Obermayer et al. 2018; Kwon et al. 2019; Schuman et al. 2019, reviewed by Huang et al. 2024) which were found throughout both sublaminae and were sometimes organized in clusters of 3-6 neurons (Figure 1D). Beside CR-cells and GABAergic interneurons, also degenerating neurons, identifiable by their shrunken and dark appearance (Figure 1A, I) were found in both sublaminae although their numbers varied substantially between brain tissue samples.

130 L1b is primarily dominated by dendritic and synaptic profiles due to a massive increase in synaptic
131 complexes (Figures 1H, 2B). Furthermore, L1b is infiltrated by apical dendrites of L2, L3 and L5 pyramidal
132 neurons interspersed with smaller dendritic segments representing apical oblique dendrites (Figures 1I, 2B).
133 The majority of synaptic complexes in L1 were axo-spinous (~80%, Figure 2 B, D, E), the remainder were
134 axo-dendritic, some of which but not all were regarded as putative GABAergic terminals (Figure 2C; but
135 see Silver et al. 2003).

136 L1b can be separated from L2 by the sudden increase of neuronal cell bodies and thick apical dendrites
137 originating at the upper pole of the somata of pyramidal neurons (Figures 1A, 2B). At the L1b and L2
138 transition more and more apical and apical oblique dendrites of different caliber were observable.

139

140 **Synaptic organization of L1 in the human TLN**

141 The primary objective of this study was to investigate the synaptic organization of excitatory SBs in L1 in
142 the human TLN, focusing on synaptic parameters that represent possible morphological correlates of
143 synaptic transmission, efficacy, strength and plasticity. The quantitative analysis was separated for both
144 sublaminae to look for possible sublaminar-specific differences. Beside the overall geometry of SBs and the
145 number and size of mitochondria, in particular the size of the PreAZ and PSD constituting the AZ, the
146 morphological equivalent to a functional neurotransmitter release site, and the organization of the three
147 functionally defined pools of SVs, namely the readily releasable (RRP), the recycling (RP) and resting pool,
148 were quantified.

149 To achieve this, a total of 361 SBs was completely reconstructed out of four patients in six series
150 containing 100-150 ultrathin sections/series. A total of 190 SBs and 184 AZs (L1a) and 171 SBs and 165
151 AZs (L1b) using neocortical access tissue (see Material and Methods; Source Data 02) were completely 3D-
152 reconstructed and quantified using fine-scale TEM, digital TEM images and subsequent 3D-volume
153 reconstructions.

154 Excitatory and inhibitory synaptic complexes in L1a und L1b were formed by either presynaptic *en*
155 *passant* or endterminal boutons with their prospective postsynaptic target structures dendritic shafts (Figures

156 2B C, D, 3A-C) or spines of different caliber and type (Figures 2B, D, E, 3A-C). In both sublaminae, SBs
157 were predominantly found on dendritic spines (~81%; L1a) and ~79% (L1b), the remainder were located
158 on dendritic shafts. The majority of SBs on spines were located on mushroom spines (L1a: ~83%, L1b:
159 ~73%), a smaller fraction on stubby spines (L1a: ~11%, L1b: ~9%) or on thin elongated spines (L1a: 6%,
160 L1b: ~22%; Figure 2E), the remainder were not classifiable.

161 Since our focus was on excitatory SBs, inhibitory terminals were not further analyzed in detail. Inhibitory
162 SBs were distinguished from excitatory SBs by their smaller SVs, which have a more spherical appearance,
163 a smaller sized PreAZ, and the lack of a prominent PSD (Figure 2D). Infrequently, GABAergic and
164 glutamatergic terminals were found on the same dendrite (Figure 2C, D) or spine (see for example Wittner
165 et al. 2001) but less frequently at ~2-3%. (Kwon et al. 2019). In turn, not all SBs located on dendritic shafts
166 were GABAergic (see for example Silver et al. 2003).

167 The ratio between excitatory vs. inhibitory SBs was between 10-15% although with layer-specific
168 differences. Our findings are in good agreement with recent publications by Shapson-Coe et al. (2024) and
169 by Cano-Astorga et al. (2023, 2024) in which the number of inhibitory SBs in different layers of the temporal
170 lobe neocortex was estimated to be10-15%. No significant differences were found in the content of
171 inhibitory SBs between the two sublaminae L1a and L1b.

172 Some SBs in both sublaminae were seen to establish either two or three synapses on the same spine,
173 spines of other origin, or dendritic shafts. Remarkably, ~90% of spines in L1a and L1b contained a spine
174 apparatus (Figure 2E), a specialized form of the endoplasmic reticulum, structures that increase spine
175 motility and may also stabilize the synaptic complex during signal transduction (Deller et al. 2003; reviewed
176 by Knott and Holtmaat 2008).

177

178 **Synaptic density in L1a and L1b of the human TLN**

179 Synaptic density measurements serve as a valuable tool for quantitatively characterizing the synaptic
180 organization of a specific cortical layer, assessing the connectivity rate, and identifying potential inter-
181 individual differences among patients within the human TLN.

182 The average density of synaptic complexes in L1 was relatively high with a value of $5.26*10^8 \pm 8.44*10^7$,
183 $5.52*10^8 \pm 1.25*10^8$ synapses/mm^3 in L1a and $5.01*10^8 \pm 1.40*10^7$ synapses/mm^3 in L1b, ranging from
184 $4.08*10^8$ to $6.31*10^8$ (L1a) and from $4.87*10^8$ to $5.15*10^8$ (L1b), respectively (Supplemental Table 1;
185 Source Data 01). Strikingly, a huge inter-individual variability was found, although with no significant
186 difference between L1a and L1b.

187 Therefore, L1 exhibited a relatively high density of synaptic complexes, indicating a relatively robust
188 and thus strong connectivity of neurons within L1 of the human TLN.

189

190 **Geometry and size of SBs and mitochondria in the human TLN**

191 Overall, L1 SBs were on average medium-sized, with a mean surface area of 5.48 ± 1.40 µm^2, and a mean
192 volume of 0.50 ± 0.19 µm^3, with a slight difference in size between L1a and L1b. Interestingly, the
193 variability in both surface area and volume of SBs was relatively small in L1a and L1b as indicated by a
194 low CV and variance (Table 1; Source Data 02) regardless of their target structures. SBs in L1 were
195 comparable in size with SBs in L5, L6, but ~2-fold larger than those in L4 of the human TLN ($p \leq 0.001$;
196 see also Yakoubi et al. 2019a, b: Schmuhl-Giesen et al. 2022).

197 Mitochondria play a pivotal role in synaptic transmission and plasticity (reviewed by Dallerac et al. 2018;
198 see also Discussion). In L1 SBs either no (Figures 2B, 3A, E) or several mitochondria (Figures 2, 3C, D;
199 range 0 to 8) of different shape and size were observed. When present, mitochondria had a volume of 0.04
200 $\pm$ 0.02 µm^3 in L1a and 0.05 ± 0.01 µm^3 in L1b, respectively (Table 1; Source Data 02). Mitochondria
201 contributed with ~7% (L1) to the total bouton volume of SBs, similar to values in L6 (~6%; Schmuhl-Giesen
202 et al. 2022), but with a ~1.5-fold lower percentage as those in L5 (~12%; Yakoubi et al. 2019a) and L4
203 (~13%; Yakoubi et al. 2019b).

204 A good correlation between the volume of the SBs and that of mitochondria was found for L1a (R^2:
205 0.7528; Figure 4B) and for L1b (R^2: 0.5992; Figure 4B). A weak correlation was also found for L6
206 (Schmuhl-Giesen et al. 2022) but a strong one in both L4 (Yakoubi et al. 2019a) and L5 (Yakoubi et al.
207 2019b) suggesting a layer-specific difference in the content of mitochondria in individual SBs.

208 **Structural composition of AZs in L1a and L1b excitatory SBs in the human TLN**

209 The number, size, and shape of the AZ, composed of the PreAZ and PSD, is one key structural determinant
210 in synaptic transmission and plasticity (Südhof 2002; Matz et al. 2010; Holderith et al. 2012) as it represents
211 the docking area of SVs (PreAZs) and the receiving area of neurotransmitter quanta at the PSD (Südhof
212 2012).

213 The majority (~98%) of SBs in L1a and L1b had only a single (Figures 2C-E, 3A-C, E) at most two or
214 three AZs (Figure 3D). Beside very large, spanning the entire pre- and postsynaptic apposition zone, also
215 smaller AZs covering only a fraction of the pre- and postsynaptic apposition zone were found.

216 On average, PreAZs were 0.18 ± 0.08 μm^2 in surface area in L1a and 0.22 ± 0.04 μm^2 in L1b with only
217 a slight variability between both sublaminae. The surface area of PSDs was quite similar to that of PreAZs
218 0.21 ± 0.01 μm^2 and was in L1a and 0.22 ± 0.05 μm^2 in L1b, respectively (Table 1; Source Data 02, sheet
219 01). Thus, the similar size of the PreAZ and PSD showed a nearly perfect overlap at the pre- and postsynaptic
220 apposition zone. L1 AZs did not show a large variability in size as indicated by the low SD, CV, and variance
221 (Table 1). Remarkably, AZs exhibited a wide range of shapes in addition to different sizes. Two types of
222 AZs were found: The majority in L1 (~80%) were of the macular and non-perforated type (Figure 3D), the
223 remainder being either horseshoe-shaped or ring-like and perforated (Figure 3E).

224 Notably, our analysis revealed only a weak correlation between the surface area of SBs and that of
225 PreAZs for L1a and L1b SBs (Figure 4A). These findings imply that the size of SBs and PreAZs is regulated
226 independently .

227 The size of the synaptic cleft (Table 1; Source Data 02, sheet 03) is an important measure at AZs since
228 its size (diameter) critically determines the temporal and spatial neurotransmitter concentration.
229 Measurements of the size of the synaptic cleft were performed on random EM images taken from the series
230 using OpenCAR or online directly at the TEM using ImageSP (Fa. Tröndle, Moorenweis, Germany). Only
231 synaptic clefts cut perpendicular to the PreAZ and PSD were included in the sample. The distance between
232 the outer edge of the PreAZ and PSD was measured at the two lateral edges and separately at the central
233 region of the synaptic cleft; the two values of the lateral edges were averaged for each cleft measurement.

234 Finally, a mean ± SD was calculated for both the lateral and central region over all synaptic clefts analyzed
235 per patient.
236 The size of the synaptic cleft did not differ significantly between the two sublaminae and was similar to
237 the results in L4, L5 (Yakoubi et al. 2019a, b) and L6.Schmuhl-Giesen et al. 2022).
238
239 **Organization of the pools of SVs in L1a and L1b excitatory SBs of the human TLN**
240 SVs are the other key structure in neurotransmitter storage and release, hence they play a fundamental role
241 in synaptic transmission and in the modulation of short- and long-term synaptic plasticity (Südhof 2002,
242 2012). Three different pools of SVs are functionally defined: the RRP, the RP, and the resting pool. Synaptic
243 efficacy, strength, mode, and probability of release (P_r) are regulated by these pools (Schikorski and Stevens
244 2001; Silver et al. 2003; Rizzoli and Betz 2004; Saviane and Silver 2006; Schikorski 2014; Watanabe et al.
245 2014; Neher 2015; Vaden et al. 2019; reviewed by Rizzoli and Betz 2005; Denker and Rizzoli 2010;
246 Chamberland and Toth 2016).
247 In general, SVs were distributed throughout the entire terminal in ~95% of the population of SBs
248 investigated (Figure 2, 3), the remainder showed a more cluster-like distribution. Two different types of
249 vesicles were found: (1) Small clear SVs with an average diameter of 25.03 ± 5.27 nm ranging up to ~40
250 nm (Table 1; Source Data 02, sheet 01). Using TEM tomography, the SV diameter was on average 30.29 ±
251 4.67 nm ranging up to ~47 nm (n = 38 SBs with a total of 5.834 SVs; Table 1; Source Data 03, sheet 05).
252 (2) DCVs (Dense Core Vesicles; Figure 3B, C, E; Source Data 02, sheet 01) with an average diameter of
253 57.97 ± 6.45 nm with no significant difference between both sublaminae. DCVs were intermingled with the
254 population of SVs throughout the entire SB (Figure 3B, C, E). DCVs play an important role in endo- and
255 exocytosis by releasing various co-transmitters, such as neuropeptides, ATP, noradrenalin, and dynorphin
256 (Ghijsen and Leenders 2005) or in synaptogenesis (Sorra et al. 2006) and the build-up of PreAZs by
257 releasing Piccolo and Bassoon (Zhai et al. 2001; Shapira et al. 2003). In addition, they are involved in
258 clustering SVs at the PreAZs (Mukherjee et al. 2010; Watanabe et al. 2014).

259 The distribution pattern of SVs made it impossible to morphologically distinguish between the three
260 functionally defined pools of SVs, with the exception of the so-called 'docked' ones, that are fused to the
261 PreAZ, and the omega-shaped bodies, that have already opened and released quanta of neurotransmitter
262 (Rizzoli and Betz, 2004; Denker and Rizzoli 2010; Neher 2015; reviewed by Rizzoli and Betz 2005;
263 Chamberland and Toth 2015). However, an attempt was made to define a morphological correlate for the
264 three functionally defined pools.

265 For this purpose, a perimeter analysis (a modified Sholl-analysis) of each SV in individual SBs was
266 carried out. The perimeter was defined as the minimum distance between each SV membrane and the PreAZ
267 membrane (Sätzler et al. 2002; for criteria to define SV pools see also Rizzoli and Betz 2005; Denker and
268 Rizzoli 2010). The putative RRP was defined as a perimeter (p) p≤10 nm and p≤20 nm to the PreAZ. These
269 criteria for the RRP from which SVs could be easily and rapidly recruited were chosen because both values
270 are less than a SV diameter apart from the PreAZ. The putative RP maintains release during moderate
271 stimulation and was classified at a distance from the PreAZ between p60-p200 nm. All SVs that were further
272 than 200 nm from the PreAZ were regarded to constitute the putative resting pool which acts as a deposit
273 of SVs only used by intense and/or repetitive stimulation.

274 On average, the total pool of SVs was 2958.62 ± 1940.51 in L1a vs. 3903.32 ± 1852.23 in L1b with an
275 average of 3430.97 ± 1773.77 for L1 (Table 1; Source Data 02). Remarkably, the total pool in L1b was
276 significantly larger ($p \leq 0.01$) by ~1.3-fold when compared to L1a. In both sublaminae (Figure 3D, E), there
277 is a huge variability in total pool size , ranging from 758 to 6542 in L1a and 1507 to 15060 in L1b, as
278 indicated by the SD, IQR and variance (Table 1). SVs contributed with ~5% (0.03 μm^3) in L1a and ~4%
279 (0.02 μm^3) in L1b to the total volume of SBs. However, no significant difference between both sublaminae
280 was observed (Table 1; Source Data 02).

281 Interestingly, no correlation between the volume of SBs vs. the total pool size was found for L1a (R^2:
282 0.2490), but a good correlation for L1b (R^2: 0.5700). Furthermore, no correlation was found between the
283 PreAZ vs. the total pool size (Figure 4C; Source Data 02).

284 The average number of SVs in the putative RRP/PreAZ for L1was 3.60 ± 4.24 SVs at p10 nm (L1a: 5.90 ±
285 5.05 SVs and L1b: 1.29 ± 1.87 SVs) with a significant difference ($p \leq 0.01$) by ~4.5-fold between the two
286 sublaminae (Table 1; Source Data 02). The putative RRP/PreAZ at the p20 nm criterion was on average
287 19.05 ±17.23 SVs (L1a: 25.04 ± 21.09 SVs and L1b: 13.07 ± 13.87 SVs) and thus nearly 2-fold larger for
288 L1a, although with a huge variability, but even though may point to sublaminae-specific differences in P_r,
289 synaptic efficacy, strength and paired-pulse behavior at individual SBs.
290 No correlation between the putative RRP at both the p10 nm and p20 nm criterion and the surface area
291 of PreAZs was found for both sublaminae. (Figure 4D, E).
292 The putative RP/PreAZ at the 60-200 nm perimeter criterion was 390.12 ± 286.89 SVs in L1a and 535.88
293 ± 321.16 in L1b with no significant difference between both sublaminae (Table 1; Source Data 02, sheet
294 01). It should be noted however, that the variability of the putative RP is relatively large in both sublaminae
295 as indicated by the SD, median, IQR and variance (Table 1).
296 Again, no correlation was observed between the SVs in the putative p60-200 nm RP and the surface area
297 of the PreAZs in both L1a (Figure 4F) and L1b (Figure 4F; Source Data 02, sheet 01).
298 The putative resting pool of SVs contained on average 2515.02 ± 1588.99 SVs in L1a and 3277.97 ±
299 1480.96 SVs in L1b with a significant difference between the two sublaminae ($p \leq 0.01$, Table 1; Source
300 Data 02, sheet 01). The number of SVs in the putative resting pool in L1b was about 1.3-fold larger when
301 compared to L1a. Again, also the putative resting pool showed a large variability for both sublaminae as
302 indicated by the SD, CV, IQR and variance (Table 1).
303 No correlation was observed between the SVs in the putative p200 nm and p500 nm resting pool and the
304 surface area of the PreAZs in L1a and L1b (Figure 4G, H; Source Data 02, sheet 01).
305 Neither for the total nor for the three different putative pools of synaptic vesicles significant differences
306 between SBs terminating on dendritic spines or shafts were found (Source Data 02, sheet 04).
307

308 **TEM tomography of L1 excitatory SBs in the human TLN**

309 It is still controversially discussed whether so-called 'docked' SVs or omega-shaped bodies represent the
310 RRP. To compare our results from the perimeter analysis for the p10 nm RRP with that of 'docked' SVs,
311 high-resolution TEM tomography was carried out. Only SBs where the AZ could be followed from its
312 beginning to its end in individual tilt-series and where the AZ was cut perpendicular through the PreAZ,
313 PSD and the synaptic cleft were analyzed. In L1a (50 SBs, on dendritic shafts = 25 SBs; on spines = 25
314 SBs) and L1b (50 SBs, on dendritic shafts = 25 SBs; on spines = 25 SBs) the number of 'docked' SVs was
315 analyzed at the PreAZ (Figure 5; Table 2; Source Data 03).

316 The results for L1a and L1b were two-fold: First, in agreement with already published results (Yakoubi
317 et al. 2019a, b; Schmuhl-Giesen et al. 2022) only in a minority (<1%) of all PreAZs analyzed, regardless of
318 their target structures, a dendritic shaft (Figure 5A) or spine (Figure 5B, C), no 'docked' SVs were observed,
319 which is in contrast to our perimeter analyses showing several boutons without vesicles within the p10 nm
320 criterion. Second, the majority of PreAZs (~98%) contained more than 2, the most 8 (L1a) and 6 (L1b)
321 'docked' SVs. This finding strongly supports multivesicular release of 'docked' SVs in L1a and L1b SBs
322 in line with findings in L4, L5 and L6 SBs (Yakoubi et al. 2019a, b; Schmuhl-Giesen et al. 2022; see also
323 Figure 5D-F).

324 On average, 3.71 ± 1.38 'docked' SVs (L1a) and 3.42 ± 1.34 'docked SVs' (L1b) were found at
325 individual PreAZs with similar values for both sublaminae. Furthermore, no significant difference was
326 found for 'docked' SVs between shaft vs. spine synapses in L1. The number of 'docked' SVs at L1a PreAZs
327 was ~2-fold smaller but nearly 3-fold larger in L1b when compared to the results of our quantitative
328 perimeter analysis for the putative RRP using the p10 nm criterion. In contrast to the p10 nm criterion with
329 high inter- and intra-individual variabilities (Suppl. Fig. 2), the number of 'docked' SVs showed a relatively
330 low variability as indicated by the SD, CV, variance, and skewness. They were different ($p \leq 0.001$) from
331 the values estimated with the p10 nm perimeter analysis.

332 There seems to be a tendency that larger PreAZs contained more 'docked' SVs providing a larger
333 'docking' area allowing the recruitment of more SVs.

334 In summary, a notable disparity difference was observed between values obtained for L1 using the p10 nm
335 criterion of the perimeter- and the TEM tomography analysis. Additionally, the putative RRP in L1 (this
336 study) and L6 (Schmuhl-Giesen et al. 2022) was ∼2-4-times smaller when compared to values in L4
337 (Yakoubi et al. 2019b) and L5 (Yakoubi et al. 2019a) pointing towards a layer-specific regulation of the
338 putative RRP. Moreover, the results suggest that not only 'docked' SVs but also those very close to the
339 PreAZ should be considered to belong to the putative RRP.
340

341 **Astrocytic coverage of L1 SBs in the human TLN**

342 Astrocytes, by directly interacting with synaptic complexes thus forming the 'tripartite' synapse play a
343 pivotal role in the induction, maintenance and termination of synaptic transmission by controlling the spatial
344 and temporal concentration of neurotransmitter quanta in the synaptic cleft (reviewed by Dellerac et al.
345 2018). Astrocytic profiles were identified by their irregular stellate shape, relatively clear cytoplasm,
346 numerous glycogen granules and bundles of intermediate filaments (for criteria see for example Peters et al.
347 1991; Ventura and Harris 1999; see also Figure 6A, B). Astrocytes and their fine processes formed a
348 relatively dense network in L4 and L5, but a comparably loose one within the neuropil in L1, as determined
349 by measuring the volume content of astrocytic processes. Astrocytic processes in L1 contributed ~20% to
350 the total human TLN volume which is similar to findings in L6 of the human TLN. The highest degree
351 (~70%) of astrocytic processes was measured in L4 (Figure 6C; Source Data 04, sheet 01, Table 3).

352 A second, more detailed measurement (Figure 6D, Table 3; source data 04, sheet 02), in which the
353 percentage of AZs covered by astrocytes was analyzed, demonstrated 1) that in L1, the majority of spine
354 and shaft synapses were not (~70%) or only partially (~20%) covered by fine astrocytic processes; 2) only
355 in a small proportion (~10%) of both spine and shaft synapses fine astrocytic processes forming a 'tripartite'
356 synapse physically isolating the synaptic complexes from the surrounding neuropil were observed; 3) the
357 results in L1 (L1a: n = 3 patients, n = 128 spine synapses, n = 48 shaft synapses; L1b: n = 3 patients, n =
358 126 spine synapses, n = 44 shaft synapses) are in contrast to those in L4 (n = 5 patients; n = 93 spine
359 synapses, n = 41 shaft synapses). In L4, a much higher number of 'tripartite' synaptic complexes (spines:

360 ~50%; shafts: ~20%) was found. In this layer, ~25% of the AZs on dendritic spines and ~60% on dendritic
361 shafts were partially covered, with large inter-individual differences. Approximately 20% of both the spine
362 and shaft synapses were not covered; 4) no significant differences between spine and shaft synapses were
363 found in either L1 or L4.

364 In summary, it is most likely that the partial coverage or complete absence of fine astrocytic processes
365 at the majority of synaptic complexes in L1 of the human TLN may contribute to different 'behaviors' of
366 synaptic complexes in synaptic transmission and in the modulation of short-term plasticity, for example in
367 the removal of 'spilled' horizontally diffusing neurotransmitter quanta favoring synaptic crosstalk (for more
368 detail see Discussion).

369

370

371 **Discussion**

372 This study investigated the synaptic organization of L1 in the human TLN. In addition to similarities, the
373 quantitative 3D models of the analyzed excitatory SBs showed significant layer-specific differences in
374 structural and synaptic parameters, in particular in the size of AZs and the total pool of SVs, the putative
375 RRP, RP, and resting pool compared to other previously studied layers (Yakoubi et al. 2019a, b; Schmuhl-
376 Giesen et al. 2022). The low degree of astrocytic coverage of L1 SBs suggests that glutamate spillover, and
377 as a consequence synaptic cross talk, may occur at most synaptic complexes in L1.

378

379 **Synaptic density measurements**

380 Synaptic density measurements are a useful tool to describe the synaptic organization of a particular area,
381 nuclei and even layers in different brain regions, but also the degree of connectivity underlying the
382 computational properties of a given brain area or in a given brain network. Meanwhile numerous studies in
383 various animal species and brain regions have performed such an analysis but data for a density of synaptic
384 complexes in humans are still rare (but see Marco and DeFelipe 1997; Tang et al. 2001; DeFelipe et al.

385 1999, 2002; Alonso-Nanclares et al. 2008; Blazquez-Llorca et al. 2013; Finnema et al. 2016; Cano-Astorga
386 et al. 2021, 2023).

387 Strikingly, a huge layer-specific difference in the mean density of synaptic contacts was found in the
388 human TLN (see also Supplemental Table 1). In L1, the overall density was $5.26*10^8 \pm 8.44*10^7$ synaptic
389 complexes/mm^3 although a great variability was observed as indicated by the SD consistent with findings
390 in the other layers of the human TLN L4 ($2.37*10^6 \pm 2.19*10^6$; Yakoubi et al. 2019b); L5 ($3.89 *10^8 \pm$
391 $9.12*10^8$; Yakoubi R., PhD Thesis 2023) and L6 ($4.98*10^7 \pm 1.85*10^7$; Schmuhl-Giesen et al. 2022) and
392 existing data published by Alonso-Nanclares et al. 2008: $9.13 \pm 0.63*10^8$ and Tang et al. 2001: $164*10^{12}$.
393 The density values for L1 and L5 are in the same order of magnitude but differ substantially from L4 and
394 L6 by one or two orders of magnitude. The huge differences in synaptic density may be explained by gender
395 and age-specific differences and the use of different methods in estimating synaptic densities (DeFelipe et
396 al. 1999).

397 In summary, the highest synaptic density was observed in L1, indicating a relatively high level of
398 connectivity and synaptic interaction. This may suggests that L1 facilitates rapid information processing
399 due to its robust synaptic activity.

400

401 **Important structural subelements of SBs in the human TLN**

402 **Shape and size of PreAZs and PSDs**

403 Synaptic efficacy, strength, modes of release and P_r are beside the pool of SVs, determined by the shape
404 and size of AZs (Matz et al. 2010; Holderith et al. 2012; Südhof 2012).

405 The majority of SBs in L1 of the human TLN had a single at most three AZs that could be of the non-
406 perforated macular or perforated type. These findings are comparable with results for other layers in the
407 human TLN (L4: Yakoubi et al. 2019b, L5: Yakoubi et al. 2019a, L6: Schmuhl-Giesen et al. 2022) but by
408 ~1.5-fold larger than in rodent and non-human primate neocortex (Marrone et al. 2005; Rollenhagen et al.
409 2015, 2018; Bopp et al. 2017; Hsu et al. 2017).

410 The surface area of AZs in L1 SBs of the human TLN was on average ~0.20 μm^2. This is in good agreement
411 with data obtained for AZs in L3 (Cano-Astorga et al. 2021), L4 (Yakoubi et al. 2019b), L5 (Yakoubi et al.
412 2019a), L6 (Schmuhl-Giesen et al. 2022) and in L3 (Cano-Astorga et al. 2023) of the human temporal and
413 cingulate neocortex. However, they were ~2- to 3-fold larger than those in mouse and non-human primates
414 visual, motor, and somatosensory neocortex (Bopp et al. 2017; Hsu et al. 2017) but remarkably even larger
415 than AZs in comparably large CNS terminals like the hippocampal mossy fiber bouton (Rollenhagen et al.
416 2007) the cerebellar mossy fiber bouton (Xu-Friedman and Regehr 2003)and the Calyx of Held in the medial
417 nucleus of the trapezoid body (Sätzler et al. 2002).

418 The substantial variability in the size of AZs at individual SBs, observed both in the human TLN and in
419 experimental animals, likely contributes to differences in synaptic efficacy, strength, P_r, quantal size, as
420 well as the size of the RRP and RP (Südhof 2002; Matz et al. 2010, Freche et al. 2011; Holderith et al. 2012;
421 Neher 2015; Chamerland and Toth 2016; Rollenhagen et al. 2018; Vaden et al. 2019; reviewed by Rizzoli
422 and Betz 2005; Denker and Rizzoli 2010). However, it has to be noted that the size of the AZ is regulated
423 as a function of activity, as shown for hippocampal SBs in the CA1 subregion (Matz et al. 2010; Holderith
424 et al. 2012). However, the comparably large size of the AZs in the human TLN also suggest a larger
425 'docking' area allowing the fusion of more SVs and thus a larger P_r.

426 It has be postulated that perforated AZs contribute to synaptic efficacy (Geinismann et al. 1992; Nava et
427 al. 2014) by an increased number of SVs at perforated synapses and plasticity (Buchs and Muller 1996;
428 Desmond and Weinberg; 1998) and by increasing the number of AMPA- and NMDA-type glutamate
429 receptors at perforated synapses (Ganeshina et al. 2004). However, since the number of perforated AZs in
430 all layers of the human TLN is relatively low compared to those of the macular-non-perforated type, it is
431 highly speculative which impact they might have here on synaptic efficacy and the modulation of synaptic
432 plasticity.

433

434

435 **Size of SVs obtained with TEM vs. TEM tomography**

436 The values obtained with both TEM (25.03 ± 5.27 nm) and TEM tomography (30.29 ± 4.67 nm) in L1 are
437 within a range published in previous studies (e.g. human TLN: Yakoubi et al. 2019a, b; Schmuhl-Giesen et
438 al. 2022; rat hippocampal CA3 region: Rollenhagen et al. 2007; Zhao et al. 2012a; rodent hippocampal CA1
439 region: Harris and Sultan 1995 [lower range]; rodent somatosensory cortex: Rollenhagen et al. 2015; 2018;
440 Prume et al. 2020). Based on TEM studies also higher mean SV diameters of ~40 nm and beyond have been
441 published for different species and brain regions (e.g. Schikorski and Stevens 1997; Sätzler et al. 2002;
442 Deak et al. 2003; Hu et al. 2008). TEM tomographic analyses also indicate variability in SV diameter from
443 ~30 to ~52 nm in different brain regions and mouse knock-out model systems (Imig et al. 2014; Muth et al.
444 2024). High variability of SV diameter have been reported to be a general phenomenon in several species
445 and brain regions, even a synapse-to-synapse variability in mean SV size is described in neighboring
446 synapses in the hippocampus, neocortex, and cerebellum of rats, mice, and human cell culture systems (Hu
447 et. al. 2008; Qu et al. 2009). Additionally, within a single SB the size of individual SVs can vary for example
448 depending on their transmitter filling state and content (e.g. Colliver et al. 2000; Pothos et al. 2002).

449

450 **Size of the three pools of SVs**

451 Besides the size of the PreAZ, the pool of rapidly releasable SVs also critically determines P_r and thus
452 synaptic efficacy, strength and plasticity (Rosenmund and Stevens 1996; Schikorski and Stevens 2001;
453 Rizzoli and Betz 2004; Schikorski 2014; Watanabe et al. 2014; Vaden et al. 2019; reviewed by Rizzoli and
454 Betz 2005, Neher 2015; Chamberland and Toth 2016). It is still rather unclear whether functionally
455 heterogeneous SV pools are structurally identifiable and thus support diverse forms of synaptic transmission
456 und would also play a pivotal role in long- and short-term plasticity. Synaptic transmission can be modulated
457 in various ways depending on the availability of SVs and on their recycling rates. Hence, the size of both
458 the RRP and RP critically determines synaptic efficacy, strength and plasticity. These parameters are
459 controlled at the PreAZ but vary substantially across various CNS synapses (reviewed by Rizzoli and Betz

460 2005; Neher 2015). The contribution of the RRP size to synaptic dynamics and the mechanisms by which
461 such control is achieved at individual SBs remains largely unknown.
462 L1-SBs had a total pool size of ~3500 SVs/AZ, larger than in other layers of the human TLN: ~2-fold in L4
463 (~1800 SVs; Yakoubi et al. 2019b), ~2.6-fold in L5 (~1350 SVs; Yakoubi et al. 2019a) and ~3-fold in L6
464 (~1150 SVs; Schmuhl-Giesen et al. 2022). Remarkably, the total pool sizes in L4 and L5 of the human TLN
465 were significantly larger than those in L4 (~550 SVs/AZ; Rollenhagen et al. 2015) and L5 (~750 SVs/AZ;
466 Rollenhagen et al. 2018) of the rat somatosensory cortex.
467 The largest total pool size in L1 may point to a pivotal role in the rapid replenishment after depletion by
468 high-frequency stimulation and the transfer of SVs into the RRP and RP from the total pool in L1 SBs.
469 The putative RRP at L1 PreAZs was on average ~4 SVs/AZ for the p10 nm RRP and similar to that in
470 L5 (~5 SVs/AZ), but significantly smaller by ~5.3-fold to that of L4 (~20 SVs/AZ) and by ~3.5-fold when
471 compared to L6 in the human TLN. Also, huge differences were observed in the putative p20 nm RRP which
472 at L1 PreAZs was ~20 SVs, ~40 SVs in L4, ~15 SVs in L5 and ~30 SVs in L6, respectively. It has to be
473 noted that a layer-specific difference in both the putative p10 nm and p20 nm RRP exists although a huge
474 variability was observed as indicated by the SD, IQR, and variance. Hence, at L1 PreAZs the overall RRP,
475 taken the p10 nm and p20 nm criterion (both together are less than a vesicle diameter) was constituted by
476 ~25 SVs rapidly available SVs that may partially contribute to the efficacy, strength and reliability of
477 synaptic transmission, but also in the modulation of short-term synaptic plasticity in L1.
478 The size of the putative RP/PreAZ was ~470 SVs in human L1 SBs and thus ~3-fold larger to that in L6
479 SBs, ~1.3- fold larger than in L4, and ~2.4-fold larger than in L5 SBs of the human TLN. In the rodent
480 neocortex the RP/PreAZ comprised ~130 (L4; Rollenhagen et al. 2015) and ~200 SVs (L5; Rollenhagen et
481 al. 2018). The comparably largest size of the RP in L1 when compared with values for the other cortical
482 layers in the human TLN and to that found for L4 and L5 in rodents may also point to a rapid availability
483 of SVs from the putative RP after the replenishment of the putative RRP during high-frequency stimulation.
484 If the refilling rates were activity dependent, the large size of the RP at L1 PreAZs could explain some forms

485 of short-term synaptic plasticity, e.g. a substantial increase in synaptic strength during frequency facilitation
486 and post-tetanic potentiation at these SBs.
487 Finally, the putative resting pool of SVs at L1 PreAZs in the human TLN is also relatively large (~3000
488 SVs) and again the largest when compared with other layers in the human TLN (L4 and L5: ~1250 SVs;
489 L6: ~900 SVs). The size of the resting pool may guarantee to rapidly replenish the RRP and RP after
490 repetitive high-frequency stimulation via active transfer of SVs with the help of mitochondria associated
491 with the pool of SVs (this study, see also Zhou and Fuster 1996; Verstreken et al. 2005; Smith et al. 2016).
492 The notable disparities in AZ and SV pool sizes among individual SBs may contribute to rapid alterations
493 in the computational properties of single neurons or networks. Consequently, these variations in AZ and SV
494 pool sizes at L1 SBs may critically influence the behavior of SBs during so-called Up-and-Down states as
495 described for other SBs of the CNS (Zhou and Fuster 1996; Sanchez-Vives and McCormick 2000; Sakata
496 and Harris 2009; Testa-Silva et al. 2014).
497
498 **Importance of presynaptic mitochondria in synaptic transmission**
499 Mitochondria in the cortical layers of the human TLN were organized in clusters associated with the pool
500 of SVs (this study, see also Yakoubi et al. 2019a, b; Schmuhl-Giesen et al. 2022). In L1, mitochondria only
501 contribute by about 7.2% (L1a) and 6.7% (L1b) to the total SB volume with similar values between L1 and
502 L6, but their percentage was ~2-fold lower than values in L4 and L5 suggesting a layer-specific distribution
503 of mitochondria in the human TLN.
504 Mitochondria play a pivotal role in the recruitment and mobilization of SVs from the RP and resting pool
505 and in the priming and docking process of SVs (Verstreken et al. 2005; Perkins et al. 2010; Smith et al.
506 2016; reviewed by Dallerac et al. 2018). In the CNS they act as the main source of internal calcium (Pozzan
507 and Rizzuto 2000; Rizzuto et al. 2000), thus they regulate and control the internal calcium concentrations
508 in CNS terminals required for the signal cascades where for example, synaptic proteins driven by Ca^{2+} like
509 synaptotagmin, synaptophysin, synaptobrevin and the SNARE-complex are involved (Südhof 2002).
510

511 **Astrocytic coverage of L1 SBS in the human TLN**

512 It is widely recognized that astrocytes play a crucial role in the formation of the 'tripartite' synapse, which
513 is a common characteristic of cortical synapses. Astrocytes serve both as a physical barrier to glutamate
514 diffusion and to mediate neurotransmitter uptake via transporters, thereby regulating the spatial and
515 temporal concentration of neurotransmitters in the synaptic cleft (Oliet et al. 2004; Min and Nevian 2012;
516 Pannasch et al. 2014; reviewed by Dallerac et al. 2018). In addition, they modulate synaptic transmission
517 by activating pre- and postsynaptic receptors (Haydon and Carmignoto 2006; Le Meur et al. 2012).
518 Moreover, it was found that the control of timing-dependent long-term depression (t-LTD) at neocortical
519 synapses is critically influenced by astrocytes by increasing Ca^{2+} signaling during the induction of t-LTD
520 (Min and Nevian 2012).

521 Remarkably, significant layer-specific differences exist in the astrocytic coverage of synaptic complexes
522 in the human TLN. Whereas in L4 and L5 ~60-80% of the total volumetric fraction was occupied by
523 astrocytic processes and most of AZs in L4 were tightly ensheathed by fine astrocytic processes, in L1 and
524 L6 the volumetric fraction of astrocytic processes was only ~20% with a loose and incomplete coverage of
525 AZs in L1 (Figure 6D). As a consequence, the lack or only incomplete astrocytic coverage of synaptic
526 complexes in L1 can only partially act as a physical barrier to neurotransmitter diffusion. In addition, beside
527 a vertical also its horizontal diffusion of glutamate at the synaptic cleft is possible. Hence, two possible
528 scenarios for the role of astrocytes are present at L1 synaptic complexes. First, as shown for only a small
529 part (10%) of synaptic complexes in L1 the 'tripartite' synapse is realized at both sides of the synaptic cleft
530 (Figure 6D). This would allow the selective uptake of horizontally diffusing glutamate via glutamate
531 transporters located in the fine astrocytic processes. This prevents 'glutamate spillover', and thus allow a
532 vertically directed neurotransmitter diffusion and docking to postsynaptic receptors at the PSD.

533 The remaining larger part of synaptic complexes in L1 either lack a coverage by fine astrocytic processes
534 at AZs or are only partially ensheathed (Figure 6D). Here 'glutamate spillover' of horizontally diffusing
535 neurotransmitter quanta is most likely and thus synaptic crosstalk between neighboring synaptic complexes
536 at AZs in neighboring spines on terminal tuft dendrites because spine density in L1 is high. This may cause

537 a switch from asynchronous to synchronous release from neighboring synaptic complexes upon repetitive
538 low- and high-frequency stimulation (von Gersdorff and Borst 2002).
539 In summary, two distinct structural scenarios were identified regarding the role of astrocytes in L1,
540 However, it is still rather unknown which of the two scenarios contribute more efficiently to synaptic
541 transmission and plasticity in L1.
542
543 **The role of L1 in the information processing of the cortical column**
544 The computational properties of the neocortex depend upon its ability to integrate the information provided
545 by the sensory organs (bottom-up information) with internally generated signals such as expectations or
546 attentional signals (top-down information). This integration occurs at apical tuft dendrites of L2/3 and L5
547 pyramidal neurons in L1. Importantly, L1 is the predominant input layer for top-down information, relayed
548 by a rich, dense network of cortico-cortical, commissural and associational long-range axonal projections.
549 In experimental animals, L1 consists exclusively of a heterogeneous population of GABAergic interneurons
550 providing feedforward and feedback inhibition (see for example Jiang et al. 2013; Boldog et al. 2018;
551 Obermayer et al. 2018; Kwon et al. 2019; reviewed by Huang et al. 2024) providing signals to the terminal
552 tuft dendrites of pyramidal neurons (reviewed by Schumann et al. 2021). In humans, there is a persistent
553 subpopulation of CR cells that provides excitation due to their long-range transcolumnar axonal projection
554 to the terminal tuft dendrites (Anstötz et al. 2014), but may also control the population of GABAergic
555 interneurons, which is as to date unknown.
556 Thus, L1 in the human neocortex is a central locus of neocortical associations controlled by excitation
557 and distinct types of inhibition (reviewed by Hartung and Letzkus 2021; Schumann et al. 2021). In summary,
558 the population of GABAergic interneurons in L1 provides inhibition and disinhibition to pyramidal terminal
559 tuft dendrites by either shunting or promoting the generation of Ca^{2+}- and Na^{+}-spikes by temporal and spatial
560 coincidence detection. Thus, the circuitry of L1, including the persistent subpopulation of excitatory CR-
561 cells; is an important and fundamental 'integrator' of the neocortex sampling bottom-up information within

562 or even across cortical columns, but also act as a ‘filter’ or ‘discriminator’ but also as an ‘amplifier’ in the
563 information processing of the neocortex.

564 Hence, L1 of the neocortex can be regarded as a complex and intricate layer of the brain serving different
565 functions, for example to gate inputs, convey expectations and context as well as mediate states of
566 consciousness, attention, cross-modal interactions, sensory perception, and learning (Bastos et al. 2012;
567 Heeger 2017; Zagha 2020; reviewed by Gilbert and Li 2013). There is evidence that L1 processing,
568 particularly Ca^{2+} signals in the distal apical dendrite, is important for sensory perception (Xu et al. 2012).

569 Recent studies have revealed that L1 plays a crucial role in top-down attentional processes, aiding in
570 directing attention, based on our goals and intentions (Hartung and Letzkus 2021; Schuman et al. 2021).
571 Additionally, L1 is implicated in the formation and consolidation of long-term memories with disruptions
572 in L1 function associated with memory deficits. Furthermore, L1 contributes to brain plasticity, which
573 involves the brain's ability to change and adapt in response to experience, including the process by which
574 synapses alter in strength and number (reviewed by Hartung and Letzkus 2021; Schuman et al. 2021).

575 Overall, L1 of the neocortex is a complex and fascinating layer of the brain that is involved in a wide
576 range of cognitive processes and brain plasticity. Since this is relayed by a network of SBs in L1, their
577 composition and connections play a pivotal role, in columnar information processing.

578

579

580 **Material and Methods**

581 Human brain tissue sampling during epilepsy surgery have been provided by Dr. med. Dorothea Miller, PD
582 Dr. med. Marec von Lehe, Department of Neurosurgery, Knappschaftschafts/Universitäts-Krankenhaus
583 Bochum and were approved by the Ethical Committees of the Rheinische Friedrich-Wilhelms-
584 University/University Hospital Bonn (Ethical votum of the Medical Faculty to Prof. Dr. med. Johannes
585 Schramm and Prof. Dr. rer. nat. Joachim Lübke, Nr. 146/11), the University of Bochum (Ethical votum of
586 the Medical Faculty to PD Dr. med. Marec von Lehe and Prof. Dr. rer. nat. Joachim Lübke, Reg. No. 5190-
587 14-15; and renewed Ethical votum of the Medical Faculty to Dr. med. Dorothea Miller and Prof. Dr. rer.

588 nat. Joachim Lübke, Reg. No. 17–6199-BR). The consent of the patients was obtained by written and signed
589 statements, and all further experimental procedures were approved by the same Ethical Committees cited
590 above, and the EU directive (2015/565/EC and 2015/566/EC) concerning working with human tissue used
591 for experimental and scientific purposes. All subsequent experimental procedures were approved by the
592 Research Committee of the Research Centre Jülich GmbH.
593
594 **Fixation and tissue processing for TEM**
595 Tissue samples from the human TLN were after their removal prepared and embedded for conventional
596 TEM and EM tomography analysis. All neocortical access tissues were obtained from patients suffering
597 from drug-resistant temporal lobe epilepsy (1 male and 3 female, 24-65 years in age for L1, and additionally
598 2 male, and 3 female, 25-63 in age for L4; see also Supplemental Table 2).
599 The pre-surgical work-up comprised high-resolution magnetic resonance imaging together with long-term
600 video-electro-encephalography (EEG)-monitoring and electrophysiology using multiple electrode
601 recordings. In all cases, the circumscribed epileptic focus was in the hippocampus proper, but not in the
602 neocortical access regions of the TL.
603 During epilepsy surgery, blocks of both non-affected, non-epileptic and epileptic neocortical access
604 tissue samples (see Supplemental Table 2) were resected and part of the tissue samples were further
605 histologically examined by neuropathologists. The non-affected non-epileptic neocortical access tissue
606 samples were always taken far from the epileptic focus and may thus be regarded as non-epileptic as also
607 demonstrated by functional studies using the same experimental approach (Mohan et al. 2015; Molnár et
608 al. 2016; Seeman et al. 2018; Obermayer et al. 2018; reviewed by Mansvelder et al. 2019). These studies
609 have clearly demonstrated that neocortical access tissue samples taken from epilepsy surgery do not differ
610 in electrophysiological properties and synaptic physiology when compared with acute slice preparations in
611 experimental animals.
612 So-called ‘post mortem’ tissue was not used in this study since the ultrastructural quality (preservation)
613 of such material is not suitable enough for fine-scale high-resolution EM, due to severe distortions of

614 relevant structural features, e.g. fragmentation and lysis of membranes of SBs, PreAZs, PSDs and SVs that
615 are required for the generation of quantitative 3D-models of SBs and their target structures (Lübke, personal
616 observation). However, under certain conditions also 'post mortem' tissue samples can be used
617 (Dominguez-Alvaro et al. 2019, 2921; Cano-Astorga et al. 2021, 2023).

618 Inter-individual differences were found in the structural and synaptic parameters analyzed as shown by
619 the box plots (Supplemental Figures 1, 2; Source Data 02).

620 Other recent studies using the same experimental approach neglected and thus discarded the effect of the
621 pharmacological treatments and disease condition (Alonso-Nanclares et al. 2008; Testa Silva et al. 2014;
622 Mohan et al. 2015; Molnár et al. 2015; Seeman et al. 2018; Dominguez-Alvaro et al. 2019; Yakoubi et al.
623 2019a, b; Schmuhl-Giesen et al. 2022).

624 For the study of L1 in the human TLN, blocks of neocortical access tissue were sampled from the
625 temporo-lateral or temporo-basal regions of the inferior temporal gyrus and the gyrus medialis. Immediately
626 after their removal during epilepsy surgery, biopsy samples of the TLN were immersion-fixed in ice-cold
627 4% paraformaldehyde and 2.5% glutaraldehyde diluted in 0.1 M phosphate buffer (PB, pH 7.4) for 24-72
628 hrs at 4°C. The fixative was replaced by fresh fixative after 2 hrs and changed twice during the subsequent
629 fixation period. Prior to vibratome sectioning, brain tissue samples were thoroughly rinsed in ice-cold PB
630 and afterwards embedded in 5% Agar-Agar (Sigma, Munich, Germany) diluted in PB.

631 Neocortical tissue blocks were cut in the coronal plane through the TLN with a Vibratome VT 1000S
632 (Leica Microsystems GmbH, Wetzlar, Germany) into 150-200 µm thick sections, collected in ice-cold PB,
633 and washed again several times in PB. Afterwards they were transferred to 0.5-1% PB-sucrose buffered
634 Osmium tetroxide (OsO_4, 300 mOsm, pH 7.4; Sigma, Munich, Germany) for 60-90 min. After visual
635 inspection to check for the quality of post-fixation, sections were thoroughly washed several times in PB
636 and left overnight at 4°C in PB. The next day they were dehydrated in an ascending series of ethanol starting
637 at 20%, 30%, 50%, 60%, 70%, 80%, 90%, 95% to absolute ethanol (15 min for each step and absolute
638 ethanol, 30 min twice), followed by a brief incubation in propylene oxide (2 min twice; Fluka, Neu-Ulm,
639 Germany). Sections were then transferred into a mixture of propylene oxide and Durcupan™ resin (2:1, 1:1

640 for 1h each; Fluka, Neu-Ulm, Germany) and stored overnight in pure resin. The next day, sections were flat
641 embedded on coated glass slides in fresh Durcupan™, coverslipped with Acla™ foils and polymerized at
642 60°C for 2 days.
643
644 **Semi- and ultrathin sectioning**
645 After light microscopic (LM) inspection, a tissue block containing the region of interest (ROI) was glued
646 on a pre-polymerized block and trimmed down. Semithin sections were cut with a Leica UltracutS
647 ultramicrotome (Leica Microsystems, Vienna, Austria), with a Histo-Diamond knife (Fa. Diatome, Nidau,
648 Switzerland). Afterwards they were briefly stained with methylene-blue (Sigma-Aldrich Chemie GmbH,
649 Taufkirchen, Germany) to identify the cortical layers, particularly L1 and underlying L2, examined and
650 documented using a motorized Olympus BX61 microscope equipped with the Olympus CellSense analysis
651 hard- and software (Olympus GmbH, Hamburg, Germany). All images were stored in a database until
652 further use.
653 After further trimming of the block to its final size, serial ultrathin sections (50 ± 5 nm thickness; silver
654 to silver gray interference contrast) were cut with a Leica UltracutS ultramicrotome through the determined
655 ROI of L1a and L1b, respectively. Ultrathin sections in serial sequence were collected on pioloform-coated
656 slot copper grids (Plano, Wetzlar, Germany). Prior to EM examination, sections were stained with 5%
657 aqueous uranyl acetate or Uranyless (Science Services, Munich, Germany) for 15–20 min and lead citrate
658 for 3–5 min according to Reynolds (1963) to enhance the contrast of biological membranes at the EM
659 level. In each series of ultrathin sections, two or three ROIs throughout L1a or L1b were chosen, and
660 photographed at a final EM magnification of 8000x with a Zeiss Libra 120 (Fa. Zeiss, Oberkochen,
661 Germany) equipped with a Proscan 2K digital camera (Fa. Tröndle, Moorenweis, Germany) using the
662 ImageSP software and its panorama function (Fa. Tröndle, Moorenweis, Germany). In addition, interesting
663 details of synaptic structures in L1a and L1b were taken at various EM magnifications.
664 All images were stored in a database until further use. Selected EM images for publication were further
665 edited using Adobe Photoshop™ and Adobe Illustrator™ software.

666 **3D-volume reconstructions and quantitative analysis of SBs**

667 EM panorama images composing each series were imported, stacked, and aligned in the reconstruction
668 software OpenCAR (Contour Alignment Reconstruction; for details see Sätzler et al. 2002). The main goal
669 of this study was to quantify several structural and synaptic parameters representing structural correlates of
670 synaptic transmission and plasticity. Excitatory SBs were characterized by large round SVs and prominent
671 PreAZs and PSDs in contrast to putative GABAergic terminals that have smaller, more oval-shaped SVs,
672 and a thin or no PSDs.

673 The following structural parameters were analyzed in randomly selected excitatory SBs: (1) surface area
674 and volume of SBs; (2) volume of mitochondria; (3) surface area of PreAZs (Dufour et al. 2016) and PSDs;
675 two apposed membrane specializations separated by the synaptic cleft; (4) number and diameter of clear
676 SVs and dense-core vesicles (DCVs); and (5) distance of individual SVs from the PreAZ for the structural
677 definition of the RRP, RP, and resting pool. 3D-volume reconstructions were generated by drawing contour
678 lines on the structures of interest in each panorama image within a series of images until a given structure
679 was completed. Presynaptic SBs, their mitochondria as well as their postsynaptic target structures were
680 outlined on the outer edge of their membranes, using closed contour lines throughout the entire stack within
681 a series. A SB was considered completely captured, when it was possible to follow the axon in both
682 directions through the entire series (*en passant* SBs) or the enlargement of the axon leading to an
683 endterminal SB. The beginning of a synaptic terminal was defined by the typical widening of the axon and
684 the abrupt occurrence of a pool of SVs.

685 The PreAZs and PSDs were regarded as complete when their perimeters were entirely reconstructed in
686 a series of ultrathin sections. The surface areas of the PreAZ and PSD were computed separately by first
687 generating a 3D surface model of the SB. The PreAZ was then measured by extracting this area from the
688 reconstructed presynaptic bouton membrane that was covered by this membrane specialization. Hence, the
689 length (L) of the PreAZ (L PreAZ) and the surface area (SA) of the PreAZ (SA PreAZ) is already known.
690 The size of the PSD opposing the PreAZ was estimated under the following assumptions: (1) both
691 membrane specializations, PreAZ and PSD run parallel to each other at the pre- and postsynaptic apposition

692 zone; (2) for both membrane specializations a contour line was drawn determining their actual length (L
693 PreAZ and L PSD). Hence, the surface area of the PSD (SA PSD) is estimated by the following equation:

694 $$\mathbf{SA\ PSD = SA\ PreAZ * L\ PSD/L\ PreAZ}$$

695 which is the perimeter ratio between the outlines of the PSD to that of the synaptic contact.
696 The synaptic cleft width was measured because of its importance for the transient temporal and spatial
697 increase of the glutamate concentration, reversible binding of glutamate to appropriate glutamate receptors
698 and eventual up-take and diffusion of glutamate out of the synaptic cleft. To a large extent, these processes
699 are governed by the geometry of this structure and the shape and size of the PreAZs and PSDs.
700 All SVs were marked throughout each SB, their diameters were individually measured and their
701 distances to the PreAZ were automatically detected using an algorithm implemented in OpenCAR (minimal
702 distance between each SV membrane to the contour line of the PreAZ) throughout the SB in every single
703 image of the series. Large DCVs were only counted in the image where they appeared largest. To avoid
704 double counts, only clear ring-like structures were counted as SVs. However, SVs might be missed in
705 densely packed regions, because ring-like traces may partly overlap. This effect may counteract any double
706 counts. Based on the small extent and the partially counteracting nature of this effect, the numbers of small
707 clear vesicles reported in this study remained uncorrected (Yakoubi et al. 2019a, b, Schmuhl-Giesen et al.
708 2022).
709 In this work, aldehyde fixation was used that is thought to induce tissue shrinkage thereby biasing
710 structural quantification (Eyre et al. 2007; Korogod et al. 2015). A direct comparison of structural
711 parameters obtained from either aldehyde or cryo-fixed and substituted tissue samples (Korogod et al.
712 2015), showed differences in cortical thickness (~16% larger in cryo-fixed material), in the volume of
713 extracellular space (~6-fold larger in cryo-fixed material), a slight increase in glial volume and overall
714 density of synaptic contacts (~14% in cryo-fixed material), but no significant differences in neuronal
715 structures such as axons, dendrites and SV diameter.
716 In the structural and synaptic parameters as estimated here, no significant difference was found for SB
717 size and other synaptic subelements such as mitochondria, active zones (AZs) and SVs when compared

718 with other studies (Zhao et al. 2012a, b). Therefore, no corrections for shrinkage were applied and we are
719 thus convinced that the synaptic parameters reported here are accurate and can be directly used for detailed
720 computational models. In addition, large-scale preservation for ultrastructural analysis will therefore
721 continue to rely on chemical fixation approaches, due to the limited preservation of the ultrastructure in
722 cryo-fixed material as stated in Korogod and co-workers (2015).
723

724 **Golgi-Cox impregnation of biopsy material in L4 of the human TLN**

725 To get an impression about the neuronal organization of the human TLN, four tissue blocks were processed
726 with the Golgi-Cox impregnation technique using the commercially available Hito Golgi-Cox OptimStain
727 kit (Hitobiotec Corp, Kingsport, TE, USA). After removal of the biopsy samples, tissues were briefly rinsed
728 twice in double distilled water (dd H_2O), and then transferred into impregnation solution 1 overnight at
729 room temperature. The next day, tissue samples were incubated in fresh impregnation solution 1 and stored
730 for 14 days in the dark at room temperature. The samples blocks were then transferred in solution 3 and
731 kept in the dark at room temperature for one day. Thereafter, they were placed into fresh solution 3 in the
732 dark at room temperature for 6 additional days. Then, solution 3 was exchanged and samples were stored
733 at 4°C in the dark overnight. Tissue blocks were embedded in 5% agarose (Carl Roth, Karlsruhe, Germany)
734 diluted in ddH_2O, and sectioned with a vibratome in the coronal plane at 100–250 µm thickness and then
735 transferred to ddH_2O.

736 After careful removal of the agarose, free-floating sections were incubated into solution 3 for 2–3 min
737 in the dark at room temperature, and right after placed into ddH_2O, washed several times and stored
738 overnight. Afterwards, they were rinsed twice in ddH_2O for 4 min each, and dehydrated in 50%, 70% and
739 95% ethanol for 5 min each, then transferred into absolute ethanol (3 × 5 min), defatted in xylene, embedded
740 in Eukitt™ (Sigma-Aldrich Chemie GmbH, Taufkirchen, Germany), finally coverslipped and air-dried.
741 Afterwards, sections were examined and imaged with an Olympus BX 61 LM equipped with the CellSense
742 software package (Olympus, Hamburg, Germany) at various magnifications and images were stored in a
743 database until further use.

744 **Stereological estimation of the density of L1 synaptic contacts in the human TLN**

745 The density of synaptic complexes, composed either between an SB with a dendrite or spine, in a given
746 volume is a valuable parameter to assess the structural and functional changes in the brain, which are linked
747 to the age, pathological or experimental conditions (Rakic et al. 1994; DeFelipe et al. 1999). The density
748 of synaptic contacts was unbiasedly estimated in L1, separated for L1a and L1b, from four patients,
749 respectively (Supplemental Table 2; Source Data 01) using the physical dissector technique (Mayhew 1996;
750 Fiala and Harris 2001) by counting the synaptic complexes in a virtual volume generated by two adjacent
751 ultrathin sections that is the dissector: the reference section and the look-up section. Here, counting was
752 performed using FIJI (Schindelin et al. 2012) on a stack of 20 aligned serial electron micrographs for each
753 patient taken from the series of ultrathin sections used for the 3D-volume reconstructions of SBs in L1. An
754 unbiased counting frame was first set and synaptic contacts to be considered (counted) are the one present
755 in the reference section only and meeting the following criteria: presence of a PreAZ and a prominent or
756 thin PSD separated by a synaptic cleft and SVs in the presynaptic terminal. Care was taken to distinguish
757 between excitatory and inhibitory synaptic contacts, as well as the postsynaptic target structures (dendritic
758 shafts or spines). Finally, the density of synaptic contacts (*Nv*) per 1 mm^3 was calculated using the formula
759 below:

760 $$\mathbf{Nv=\sum Qd/\sum Vd}$$

761 where *Qd* is the number of synaptic contacts per dissector and Vd is the volume of the dissector given by:
762 Number of dissectors x frame area x section thickness.

763

764 **TEM tomography of L1 SBs in the human TLN**

765 EM tomography was performed on 200-300 nm thick sections cut from blocks prepared for serial ultrathin
766 sectioning as described above (Table 2; Source Data 03). Sections were mounted on pioloform-coated line
767 copper grids and were counterstained with uranyl acetate and lead citrate following a slightly modified
768 staining protocol as described by Reynolds (1963).

769 Subsequently, sections were examined with a JEOL JEM 1400Plus, operating at 120 kV and equipped with
770 a 4096×4096 pixels CMOS camera (TemCam-F416, TVIPS, Gauting, Germany). Tilt-series were acquired
771 automatically over an angular range of −60° to +60° at 1°-degree increments using Serial EM (Mastronarde
772 2005). Stack alignment and reconstruction by filtered backprojection were carried out using the software
773 package iMOD (Kremer et al. 1996). Final reconstructions were ultimately filtered using a median filter
774 with a window size of 3 pixels. Tilt-series were stored as .tif files and were further processed using the
775 freely available software Imod 4.9.12 and ImageJ (ImageJ, RRID:SCR-0033070). In each tilt-series so-
776 called 'docked' SVs identified by their fusion with the PreAZ or as omega-shaped body that already
777 released a quantum of neurotransmitter were counted separately for L1a and L1b and for their target
778 structures, dendritic shafts or spines in randomly selected SBs.

779 To determine possible differences to the values obtained by the 3D-reconstructions, in the same tilt-series
780 binned at 24 nm (section thickness) the diameter of SVs was measured randomly by using OpenCAR as
781 described above. To avoid double counts and underestimations of the diameter, the ring-shaped structure of
782 an SV was compared on each tilted-slice and only marked if it appears largest. In 18 tilt-series each consisting
783 of 9-14 tilt-slices, randomly selected SBs were investigated (L1a: 8 tilt series; 16 SBs with a total of 2094
784 SVs; L1b: 10 tilt series; 22 SBs with a total of 3740 SVs).

785

786 **Quantitative analysis of the astrocytic coverage**

787 Although methodologically associated with the possibility of a certain degree of error, astrocytic processes
788 around synaptic complexes were mainly identified by their relatively clear cytoplasm compared to synaptic
789 boutons or dendritic profiles; in addition by their irregular, stellate shape, by the presence of glycogen
790 granules and bundles of intermediate filaments (Peters et al. 1991; Ventura and Harris 1999). With greater
791 accuracy, astrocytic processes can be identified with immunolabeling, but this leads to poorer tissue
792 preservation and resolution of cellular structures such as AZs. Among studies in rats (e.g. Rollenhagen et
793 al. 2015; 2018) in a previous study on the human TLN (Yakoubi et al. 2019a) immunohistochemistry against
794 glutamine synthetase, a key enzyme in astrocytes, was carried out. Since similar results were obtained

795 without immunohistochemistry when identifying astrocytic processes around AZs, immunohistochemistry
796 was omitted in the series of follow-up studies on the human TLN.

797 To quantify the volume contribution of astrocytic processes in the human neocortex, the interactive
798 software ImageJ (Schneider et al. 2012) was used. The first, the middle, and the last images of an individual
799 EM series were used for a further quantitative volumetric analysis (Source Data 04, sheet 01). In each section
800 of the same series used for the 3D-volume reconstructions, a grid (grid size 1×1 μm^2) was placed over the
801 EM image, and in each square, the abundance of fine astrocytic processes was documented throughout these
802 images and averaged. Using the Cavalieri method [Unbiased Stereology: Three-Dimensional Measurement
803 in Microscopy (Advanced Methods) Paperback-January 7, 2005, by Vyvyan Howard Matthew Reed], the
804 (absolute) volume contribution of astrocytic processes was determined according to the Cavalieri estimator:

805 $$\mathbf{V=a(p)\times\Sigma P\times t}$$

806 where a(p) is the size of one square (0.8×0.8 μm2), P is the number of squares counted, and t is the
807 thickness of the slice.

808 In addition, in consecutive sections spanning the complete AZ , the astrocytic coverage was evaluated
809 under the following criteria: fine astrocytic processes were observed on 1) both sides of the AZ reaching as
810 far as the synaptic cleft, 2) only one side of the AZ was covered by fine astrocytic processes and 3) AZs
811 without astrocytic processes (Source Data 04, sheet 02). Values obtained for L1 (L1a: n = 3 patients; L1b:
812 3 patients) either for SBs terminating on dendritic spines (L1a: n = 128; L1b: n=126) or shafts (L1a: n= 48;
813 L1b: n = 44) were compared to L4 (n = 5 patients; dendritic spines n=93; dendritic shafts n=41). Layer 4
814 was chosen because the volumetric analysis showed the highest portion of astrocytic processes in this layer
815 compared to all other cortical layers. All values are given as percentages.

816

817 **Statistical analysis**

818 The mean value ± standard deviation (SD), the median with the interquartile range (IQR), the coefficient
819 of variation (CV), skewness, variance, and the coefficient of correlation (R^2) were given for each structural
820 parameter analyzed. The p-value was considered significant only if $p < 0.05$. Box- and Violin plots (Plotly

821 4.0.0 https://chart-studio.plotly.com) were generated to investigate inter-individual differences for each
822 patient and structural parameter (Supplemental Figure 1, 2; Source Data 02).
823 To test for significant differences, the non-parametric Kruskal-Wallis H-test with a subsequent Mann-
824 Whitney u-test analysis was performed, using PAST 4.02 (Hammer et al. 2001). Correlation graphs between
825 several structural parameters were then generated (Figure 4). The R^2-values were interpreted as follows: 0,
826 no linear correlation; 0-0.5, weak linear correlation; 0.5-0.8, good linear correlation; and 0.8-1.0, strong
827 linear correlation. Furthermore, a freely available Fisher's *r*-to-*z*-transformation calculator (Fisher's z) was
828 used to test for differences in R^2 between L1a and L1b (p-value < 0.05). For statistical comparison with
829 other layers of the human TLN, L1a and L1b were grouped together as L1.
830 Parts of the data acquisition were carried out in the context of a PhD Thesis (Sadeghi Dastjerdi A.
831 2024).Values obtained in the present study for L1 were compared partially to those obtained for L2, L3
832 (Girwert Ch., PhD Thesis in preparation), L4, L5 (Yakoubi et al. 2019a, b; Yakoubi R., PhD Thesis 2023)
833 and L6 (Schmuhl-Giesen et al. 2022).
834
835
836
837 **Acknowledgments**
838 We would like to thank our technicians Brigitte Marshallsay and Tayfun Palaz for their excellent technical
839 assistance. Furthermore, the constant financial support of the Helmholtz Society is very much
840 acknowledged.
841

842 **References**

843 Allone, C., Lo Buono, V., Corallo, F., Pisani, L.R., Pollicino, P., Bramanti, P., and Marino, S. (2017).
844 Neuroimaging and cognitive functions in temporal lobe epilepsy: A review of the literature. J. Neurol. Sci.
845 381, 7-15. 10.1016/j.jns.2017.08.007.

846 Alonso-Nanclares, L., Gonzalez-Soriano, J., Rodriguez, J.R., and DeFelipe, J. (2008). Gender differences
847 in human cortical synaptic density. Proc. Natl. Acad. Sci. USA 105, 14615-14619.
848 10.1073/pnas.0803652105.

849 Anstötz, M., Cosgrove, K.E., Hack, I., Mugnaini, E., Maccaferri, G., Lübke, J.H.R. (2014), Morphology,
850 input-output relations and synaptic connectivity of Cajal-Retzius cells in layer 1 of the developing neocortex
851 of CXCR4-EGFP mice. Brain Struct. Funct. 219, 2119-2139. 10.1007/s00429-013-0627-2.

852 Bastos, A.M., Usrey, W.M., Adams, R.A., Mangun, G.R., Fries, P., and Friston, K.J. (2012). Canonical
853 microcircuits for predictive coding. Neuron 76, 695-711. 10.1016/j.neuron.2012.10.038.

854 Blazquez-Llorca, L., Merchan-Perez, A., Rodriguez, J.R., Gascon, J., and DeFelipe, J. (2013). FIB/SEM
855 technology and Alzheimer's disease: three-dimensional analysis of human cortical synapses. J. Alzheimers
856 Dis. 34, 995-1013. 10.3233/JAD-122038.

857 Boldog, E., Bakken, T.E., Hodge, R.D., Novotny, M., Aevermann, B.D., Baka, J., Borde, S., Close, J.L., et
858 al. (2018). Transcriptomic and morphophysiological evidence for a specialized human cortical GABAergic
859 cell type. Nat. Neurosci. 21,1185-1195.

860 Bopp, R., Holler-Rickauer, S., Martin, K.A.C., and Schuhknecht, G.F. (2017). An Ultrastructural Study of
861 the Thalamic Input to Layer 4 of Primary Motor and Primary Somatosensory Cortex in the Mouse. J.
862 Neurosci. 37, 2435-2448. 10.1523/JNEUROSCI.2557-16.2017.

863 Buchs, P.A., Muller, D. (1996), Induction of long-term potentiation is associated with major ultrastructural
864 changes of activated synapses. Proc. Natl. Acad. Sci. USA 93, 8040-8045.

865 Bystron, I., Blakemore, C., and Rakic, P. (2008). Development of the human cerebral cortex: Boulder
866 Committee revisited. Nat. Rev. Neurosci. 9, 110-122. 10.1038/nrn2252.

867 Cajal, S.R. (1911). Histology of the nervous system of man and vertebrates. History of Neuroscience
868 (Oxford Univ Press, New York, 1995).

869 Cano-Astorga, N., DeFelipe, J., and Alonso-Nanclares, L. (2021). Three-Dimensional Synaptic
870 Organization of Layer III of the Human Temporal Neocortex. Cereb. Cortex 31, 4742-4764.
871 10.1093/cercor/bhab120.

872 Cano-Astorga N, Plaza-Alonso S, DeFelipe J, Alonso-Nanclares L (2023), 3D synaptic organization of layer
873 III of the human anterior cingulate and temporopolar cortex. Cereb. Cortex 33, 9691-9708.
874 10.1093/cercor/bhad232.

875 Cano-Astorga N, Plaza-Alonso S, Turegano-Lopez M, Rodrigo-Rodriguez J, Merchan-Perez A, DeFelipe
876 J. (2024). Unambiguous identification of asymmetric and symmetric synapses using volume electron
877 microscopy. Front Neuroanat 18:1348032.

878 Chamberland, S., and Toth, K. (2016). Functionally heterogeneous synaptic vesicle pools support diverse
879 synaptic signalling. J. Physiol. 594, 825-835. 10.1113/JP270194.

880 Colliver TL, Pyott SJ, Achalabun M, Ewing AG. 2000. VMAT-Mediated changes in quantal size and
881 vesicular volume. J Neurosci 20:5276-5282.

882 Cooper, J.A. (2008). A mechanism for inside-out lamination in the neocortex. Trends Neurosci. 31, 113-
883 119. 10.1016/j.tins.2007.12.003

884 Dallerac, G., Zapata, J., and Rouach, N. (2018). Versatile control of synaptic circuits by astrocytes: where,
885 when and how? Nat. Rev. Neurosci. 19, 729-743. 10.1038/s41583-018-0080-6.

886 Deak F, Schoch S, Liu X, Südhof TC, Kavalali ET. 2004. Synaptobrevin is essential for fast synaptic-vesicle
887 endocytosis. Nat Cell Biol 6:1102-1108.

888 DeFelipe, J., Marco, P., Busturia, I., and Merchan-Perez, A. (1999). Estimation of the number of synapses
889 in the cerebral cortex: methodological considerations. Cereb. Cortex 9, 722-732. 10.1093/cercor/9.7.722.

890 DeFelipe, J., Oroquieta, J., Arellano, J.I., Alonso, L., and Munoz, A. (2002). The neuropathology of
891 temporal lobe epilepsy: primary and secondary changes in the cortical circuits and epileptogenicity. Rev.
892 Neurol. 34, 401-408.

893 Deller, T., Korte, M., Chabanis, S., Drakew, A., Schwegler, H., Stefani, G.G., Zuniga, A., Schwarz, K.,
894 Bonhoeffer, T., Zeller, R., et al. (2003). Synaptopodin-deficient mice lack a spine apparatus and show
895 deficits in synaptic plasticity. Proc. Natl. Acad. Sci. USA 100, 10494-10499. 10.1073/pnas.1832384100.

896 Denker, A., and Rizzoli, S.O. (2010). Synaptic vesicle pools: an update. Front. Synaptic. Neurosci. 2, 135.
897 10.3389/fnsyn.2010.00135.

898 Desmond, N.L., Weinberg, R.J. (1998), Enhanced expression of AMPA receptor protein at perforated
899 axospinous synapses. Neuroreport. 9, 857-860.

900 Dominguez-Alvaro, M., Montero-Crespo, M., Blazquez-Llorca, L., DeFelipe, J., and Alonso-Nanclares, L.
901 (2019). 3D Electron Microscopy Study of Synaptic Organization of the Normal Human Transentorhinal
902 Cortex and Its Possible Alterations in Alzheimer's Disease. eNeuro 6. 10.1523/ENEURO.0140-19.2019

903 Dominguez-Alvaro, M., Montero-Crespo, M., Blazquez-Llorca, L., DeFelipe, J., and Alonso-Nanclares, L.
904 (2021). 3D Ultrastructural Study of Synapses in the Human Entorhinal Cortex. Cereb. Cortex 31, 410-425.
905 10.1093/cercor/bhaa233.

906 Dufour, A., Rollenhagen, A., Sätzler, K., and Lübke, J.H.R. (2016). Development of Synaptic Boutons in
907 Layer 4 of the Barrel Field of the Rat Somatosensory Cortex: A Quantitative Analysis. Cereb. Cortex 26,
908 838-854. 10.1093/cercor/bhv270.

909 Economo, C. F. von and Koskinas, G. N. (1925) Die Cytoarchitektonik der Hirnrinde des erwachsenen
910 Menschen, J. Springer, Berlin und Wien. 10.1007/978-3-642-37824-9.

911 Eyre, M.D., Freund, T.F., and Gulyas, A.I. (2007). Quantitative ultrastructural differences between local
912 and medial septal GABAergic axon terminals in the rat hippocampus. Neuroscience 149, 537-548.
913 10.1016/j.neuroscience.2007.08.006.

914 Fiala, J.C., and Harris, K.M. (2001). Extending unbiased stereology of brain ultrastructure to three-
915 dimensional volumes. J. Am. Med. Inform. Assoc. 8, 1-16. 10.1136/jamia.2001.0080001.

916 Finnema, S.J., Nabulsi, N.B., Eid, T., Detyniecki, K., Lin, S.F., Chen, M.K., Dhaher, R., Matuskey, D.,
917 Baum, E., Holden, D., et al. (2016). Imaging synaptic density in the living human brain. Sci. Transl. Med.
918 8, 348-396. 10.1126/scitranslmed.aaf66.

919 Freche, D., Pannasch, U., Rouach, N., and Holcman, D. (2011). Synapse geometry and receptor dynamics
920 modulate synaptic strength. PLoS One *6*, e25122. 10.1371/journal.pone.0025122.

921 Ganeshina, O., Berry, R.W., Petralia, R.S., Nicholson, D.A., Geinisman, Y. (2004), Differences in the
922 expression of AMPA and NMDA receptors between axospinous perforated and nonperforated synapses are
923 related to the configuration and size of postsynaptic densities. J. Comp. Neurol. 468, 86-95.

924 Geinisman, Y., Morrell. F., deToledo-Morrell, L. (1992), Increase in the number of axospinous synapses
925 with segmented postsynaptic densities following hippocampal kindling. Brain Res. 569, 341-347.

926 Ghijsen, W.E., and Leenders, A.G. (2005). Differential signaling in presynaptic neurotransmitter release.
927 Cell. Mol. Life Sci. 62, 937-954. 10.1007/s00018-004-4525-0.

928 Gilbert, C.D., and Li, W. (2013). Top-down influences on visual processing. Nat. Rev. Neurosci. 14, 350-
929 363. 10.1038/nrn3476.

930 Hartung, J., and Letzkus, J.J. (2021). Inhibitory plasticity in layer 1 - dynamic gatekeeper of neocortical
931 associations. Curr. Opin. Neurobiol. 67, 26-33. 10.1016/j.conb.2020.06.003.

Hammer, Ø., Harper, A.T., and Ryan P.D. (2001). Past: paleontological statistics software package for education and data analysis. Palaeontologia Electronica. 4, 1–9; https://palaeo-electronica.org/2001_1/past/issue1_01.htm.

Harris KM, Sultan P. 1995. Variation in the number, location and size of synaptic vesicles provides an anatomical basis for the nonuniform probability of release at hippocampal CA1 synapses. Neuropharmacology 34:1387-1395.

Haydon, P.G., and Carmignoto, G. (2006). Astrocyte control of synaptic transmission and neurovascular coupling. Physiol. Rev. 86, 1009-1031. 10.1152/physrev.00049.2005.

Heeger, D.J. (2017). Theory of cortical function. Proc. Natl. Acad. Sci. USA 114, 1773-1782. 10.1073/pnas.1619788114.

Holderith, N., Lorincz, A., Katona, G., Rozsa, B., Kulik, A., Watanabe, M., and Nusser, Z. (2012). Release probability of hippocampal glutamatergic terminals scales with the size of the active zone. Nat. Neurosci. 15, 988-997. 10.1038/nn.3137.

Hsu, A., Luebke, J.I., and Medalla, M. (2017). Comparative ultrastructural features of excitatory synapses in the visual and frontal cortices of the adult mouse and monkey. J. Comp. Neurol. 525, 2175-2191. 10.1002/cne.24196.

Hu Y, Qu L, Schikorski T. 2008. Mean synaptic vesicle size varies among individual excitatory hippocampal synapses. Synapse 62:953-957.

Huang S, Wu SJ, Sansone G, Ibrahim LA, Fishell G. 2024. Layer 1 neocortex: Gating and integrating multidimensional signals. Neuron 112:184-200.

Imig C, Min SW, Krinner S, Arancillo M, Rosenmund C, Sudhof TC, Rhee J, Brose N, Cooper BH. 2014. The morphological and molecular nature of synaptic vesicle priming at presynaptic active zones. Neuron 84:416-431.

Insausti, R. (2013). Comparative neuroanatomical parcellation of the human and nonhuman primate temporal pole. J. Comp. Neurol. 521, 4163-4176. 10.1002/cne.23431.

Jiang, X., Wang, G., Lee, A.J., Stornetta, R.L., and Zhu, J.J. (2013). The organization of two new cortical interneuronal circuits. Nat. Neurosci. 16, 210-218. 10.1038/nn.3305.

Kiernan, J.A. (2012). Anatomy of the temporal lobe. Epilepsy Res. Treat 2012, 176157. 10.1155/2012/176157.

Knott, G., and Holtmaat, A. (2008). Dendritic spine plasticity--current understanding from in vivo studies. Brain Res. Rev. 58, 282-289. 10.1016/j.brainresrev.2008.01.002.

963 Korogod, N., Petersen, C.C., and Knott, G.W. (2015). Ultrastructural analysis of adult mouse neocortex
964 comparing aldehyde perfusion with cryo fixation. Elife 4. 10.7554/eLife.05793.

965 Kremer, J.R., Mastronarde, D.N., and McIntosh, J.R. (1996). Computer visualization of three-dimensional
966 image data using IMOD. J. Struct. Biol. 116, 71-76. 10.1006/jsbi.1996.0013.

967 Kwon, T., Merchan-Perez, A., Rial Verde, E.M., Rodriguez, J.R., DeFelipe, J., Yuste, R. (2019),
968 Ultrastructural, Molecular and Functional Mapping of GABAergic Synapses on Dendritic Spines and Shafts
969 of Neocortical Pyramidal Neurons. Cerebral Cortex 29, 2771-2781.

970 Le Meur, K., Mendizabal-Zubiaga, J., Grandes, P., and Audinat, E. (2012). GABA release by hippocampal
971 astrocytes. Front. Comput. Neurosci. 6, 59. 10.3389/fncom.2012.00059.

972 Luskin, M.B., and Shatz, C.J. (1985a). Neurogenesis of the cat's primary visual cortex. J. Comp. Neurol.
973 242, 611-631. 10.1002/cne.902420409.

974 Luskin, M.B., and Shatz, C.J. (1985b). Studies of the earliest generated cells of the cat's visual cortex:
975 cogeneration of subplate and marginal zones. J. Neurosci. 5, 1062-1075. 10.1523/JNEUROSCI.05-04-
976 01062.1985.

977 Lübke, J., and Feldmeyer D (2007). Excitatory signal flow and connectivity in a cortical column: focus on
978 barrel cortex. Brain Struct Funct 212, 3-17. 10.1007/s00429-007-0144-2.

979 Mansvelder, H.D., Verhoog, M.B., and Goriounova, N.A. (2019). Synaptic plasticity in human cortical
980 circuits: cellular mechanisms of learning and memory in the human brain? Curr. Opin. Neurobiol. 54, 186-
981 193. 10.1016/j.conb.2018.06.013.

982 Marco, P., and DeFelipe, J. (1997). Altered synaptic circuitry in the human temporal neocortex removed
983 from epileptic patients. Exp. Brain Res. 114, 1-10. 10.1007/pl00005608.

984 Marin-Padilla, M. (1978). Dual origin of the mammalian neocortex and evolution of the cortical plate. Anat.
985 Embryol. (Berl) 152, 109-126. 10.1007/BF00315920.

986 Marin-Padilla M. (1998). Cajal-Retzius cells and the development of the neocortex. Trends Neurosci 21:64-
987 71.

988 Marrone, D.F., LeBoutillier, J.C., and Petit, T.L. (2005). Ultrastructural correlates of vesicular docking in
989 the rat dentate gyrus. Neurosci. Lett. 378, 92-97. 10.1016/j.neulet.2004.12.019.

990 Martinez-Cerdeno, V., Noctor, S.C. (2014), Cajal, Retzius, and Cajal-Retzius cells. Front. Neuroanat. 8, 48.

991 Mastronarde DN. 2005. Automated electron microscope tomography using robust prediction of specimen
992 movements. J Struct Biol 152:36-51.

993 Matz, J., Gilyan, A., Kolar, A., McCarvill, T., and Krueger, S.R. (2010). Rapid structural alterations of the
994 active zone lead to sustained changes in neurotransmitter release. Proc. Natl. Acad. Sci. USA 107, 8836-
995 8841. 10.1073/pnas.0906087107.

996 Mayhew, T.M. (1996). How to count synapses unbiasedly and efficiently at the ultrastructural level:
997 proposal for a standard sampling and counting protocol. J. Neurocytol. 25, 793-804. 10.1007/BF02284842.

998 Min, R., and Nevian, T. (2012). Astrocyte signaling controls spike timing-dependent depression at
999 neocortical synapses. Nat. Neurosci. 15, 746-753. 10.1038/nn.3075.

1000 Mohan, H., Verhoog, M.B., Doreswamy, K.K., Eyal, G., Aardse, R., Lodder, B.N., Goriounova, N.A.,
1001 Asamoah, B., AB, B.B., Groot, C., et al. (2015). Dendritic and Axonal Architecture of Individual Pyramidal
1002 Neurons across Layers of Adult Human Neocortex. Cereb. Cortex 25, 4839-4853. 10.1093/cercor/bhv188.

1003 Molnár, G., Rozsa, M., Baka, J., Holderith, N., Barzo, P., Nusser, Z., and Tamas, G. (2016). Human
1004 pyramidal to interneuron synapses are mediated by multi-vesicular release and multiple docked vesicles.
1005 Elife 5. 10.7554/eLife.18167.

1006 Mukherjee, K., Yang, X., Gerber S.H., Kwon, H.B., Ho, A., Castillo, P.E., Liu, X., and Südhof, T.C. (2010).
1007 Piccolo and bassoon maintain synaptic vesicle clustering without directly participating in vesicle exocytosis.
1008 Proc. Natl. Acad. Sci. USA, 107, 6504-6509. 10.1073/pnas.1002307107.

1009 Muth S, Moschref F, Freckmann L, Mutschall S, Hojas-Garcia-Plaza I, Bahr JN, Petrovic A, Thanh Thao
1010 D, Schwarze V, Archit A, Weyand K, Michanski S, Maus L, Imig C, Brose N, Wichmann C et al. (2024).
1011 SynapseNet: Deep Learning for Automatic Synapse Reconstruction. bioRxiv preprint doi:
1012 https://doi.org/10.1101/2024.12.02.626387.

1013 Nava, N., Chen, F., Wegener, G., Popoli. M., Nyengaard, J.R. (2014), A new efficient method for synaptic
1014 vesicle quantification reveals differences between medial prefrontal cortex perforated and nonperforated
1015 synapses. J. Comp. Neurol. 522, 284-297.

1016 Neher, E. (2015). Merits and Limitations of Vesicle Pool Models in View of Heterogeneous Populations of
1017 Synaptic Vesicles. Neuron 87, 1131-1142. 10.1016/j.neuron.2015.08.038.

1018 Obermayer, J., Heistek, T.S., Kerkhofs, A., Goriounova, N.A., Kroon, T., Baayen, J.C., Idema, S., Testa-
1019 Silva, G., Couey, J.J., and Mansvelder, H.D. (2018). Lateral inhibition by Martinotti interneurons is
1020 facilitated by cholinergic inputs in human and mouse neocortex. Nat. Commun. 9, 4101. 10.1038/s41467-
1021 018-06628-w.

1022 Oliet, S.H.R., Piet, R., Poulain, D.A., and Theodosis, D.T. (2004). Glial modulation of synaptic
1023 transmission: Insights from the supraoptic nucleus of the hypothalamus. Glia 47, 258-267.
1024 10.1002/glia.20032.

1025 Palomero-Gallagher, N., and Zilles, K. (2019). Cortical layers: Cyto-, myelo-, receptor- and synaptic
1026 architecture in human cortical areas. Neuroimage 197, 716-741. 10.1016/j.neuroimage.2017.08.035.

1027 Pannasch, U., Freche, D., Dallerac, G., Ghezali, G., Escartin, C., Ezan, P., Cohen-Salmon, M., Benchenane,
1028 K., Abudara, V., Dufour, A., et al. (2014). Connexin 30 sets synaptic strength by controlling astroglial
1029 synapse invasion. Nat. Neurosci. 17, 549-558. 10.1038/nn.3662.

1030 Peters, A., Josephson, K., Vincent, S.L. (1991), Effects of aging on the neuroglial cells and pericytes within
1031 area 17 of the rhesus monkey cerebral cortex. Anat. Rec. 229, 384-398.

1032 Perkins, G.A., Tjong, J., Brown, J.M., Poquiz, P.H., Scott, R.T., Kolson, D.R., Ellisman, M.H., and Spirou,
1033 G.A. (2010). The micro-architecture of mitochondria at active zones: electron tomography reveals novel
1034 anchoring scaffolds and cristae structured for high-rate metabolism. J. Neurosci. 30, 1015-1026.

1035 Pothos EN, Mosharov E, Liu KP, Setlik W, Haburcak M, Baldini G, Gershon MD, Tamir H, Sulzer D. 2002.
1036 Stimulation-dependent regulation of the pH, volume and quantal size of bovine and rodent secretory
1037 vesicles. J Physiol 542:453-476.

1038 Pozzan, T., and Rizzuto, R. (2000). The renaissance of mitochondrial calcium transport. Eur. J. Biochem.
1039 267, 5269-5273. 10.1523/JNEUROSCI.1517-09.2010.

1040 Prume, M., Rollenhagen, A., Yakoubi, R., Sätzler, K., and Lübke, J.H. (2020). Quantitative Three-
1041 Dimensional Reconstructions of Excitatory Synaptic Boutons in the "Barrel Field" of the Adult "Reeler"
1042 Mouse Somatosensory Neocortex: A Comparative Fine-Scale Electron Microscopic Analysis with the Wild
1043 Type Mouse. Cereb. Cortex 30, 3209-3227. 10.1093/cercor/bhz304.

1044 Qu L, Akbergenova Y, Hu Y, Schikorski T. 2009. Synapse-to-synapse variation in mean synaptic vesicle
1045 size and its relationship with synaptic morphology and function. J Comp Neurol 514:343-352.

1046 Rakic, P., Bourgeois, J.P., and Goldman-Rakic, P.S. (1994). Synaptic development of the cerebral cortex:
1047 implications for learning, memory, and mental illness. Prog. Brain Res. 102, 227-243. 10.1016/S0079-
1048 6123(08)60543-9.

1049 Reynolds, E.S. (1963), The use of lead citrate at high pH as an electron-opaque stain in electron microscopy.
1050 J Cell Biol 17, 208-212. 10.1083/jcb.17.1.208.

1051 Retzius, G. (1893). Die Cajal'schen Zellen der Grosshirnrinde beim Menschen und bei Säugerthieren. Biol.
1052 Untersuchungen 5, 1.

1053 Retzius, G. (1894). Weitere Beitrage zur Kenntniss der Cajal'schen Zellen der Grosshirnrinde des
1054 Menschen. Biol. Untersuchungen 6, 29–34

1055 Rizzoli, S.O., and Betz, W.J. (2004). The structural organization of the readily releasable pool of synaptic
1056 vesicles. Science 303, 2037-2039. 10.1126/science.1094682.

1057 Rizzoli, S.O., and Betz, W.J. (2005). Synaptic vesicle pools. Nat. Rev. Neurosci. 6, 57-69. 10.1038/nrn1583.

1058 Rizzuto, R., Bernardi, P., and Pozzan, T. (2000). Mitochondria as all-round players of the calcium game. J.
1059 Physiol. *529*, 37-47. 10.1111/j.1469-7793.2000.00037.x.

1060 Rockland, K.S., and DeFelipe, J. (2018). Editorial: Why Have Cortical Layers? What Is the Function of
1061 Layering? Do Neurons in Cortex Integrate Information Across Different Layers? Front. Neuroanat. 12, 78.
1062 10.3389/fnana.2018.00078.

1063 Rollenhagen, A., Sätzler, K., Rodriguez, E.P., Jonas, P., Frotscher, M., and Lübke, J.H. (2007). Structural
1064 determinants of transmission at large hippocampal mossy fiber synapses. J. Neurosci. 27, 10434-10444.
1065 10.1523/JNEUROSCI.1946-07.2007.

1066 Rollenhagen, A., Klook, K., Sätzler, K., Qi, G., Anstötz, M., Feldmeyer, D., and Lübke, J.H.R. (2015).
1067 Structural determinants underlying the high efficacy of synaptic transmission and plasticity at synaptic
1068 boutons in layer 4 of the adult rat 'barrel cortex'. Brain Struct. Funct. 220, 3185-3209. 10.1007/s00429-014-
1069 0850-5.

1070 Rollenhagen, A., Ohana, O., Sätzler, K., Hilgetag, C.C., Kuhl, D., and Lübke, J.H.R. (2018). Structural
1071 Properties of Synaptic Transmission and Temporal Dynamics at Excitatory Layer 5B Synapses in the Adult
1072 Rat Somatosensory Cortex. Front. Synaptic. Neurosci. 10, 24. 10.3389/fnsyn.2018.00024.

1073 Rosenmund, C., and Stevens, C.F. (1996). Definition of the readily releasable pool of vesicles at
1074 hippocampal synapses. Neuron 16, 1197-1207. 10.1016/s0896-6273(00)80146-4.

1075 Sadeghi Dastjerdi, A. (2024) Ultrastructural sublamina-specific diversity of excitatory synaptic boutons in
1076 layer 1 in the adult human temporal lobe neocortex: a qualitative and quantitative electron microscopic
1077 analysis. PhD Thesis RWTH Aachen; DOI: 10.18154/RWTH-2024-01652.

1078 Sätzler K, Söhl LF, Bollmann JH, Borst JG, Frotscher M, Sakmann B, Lübke JH. 2002. Three-dimensional
1079 reconstruction of a calyx of Held and its postsynaptic principal neuron in the medial nucleus of the trapezoid
1080 body. J Neurosci 22:10567-10579.

1081 Sakata, S., and Harris, K.D. (2009). Laminar structure of spontaneous and sensory-evoked population
1082 activity in auditory cortex. Neuron 64, 404-418. 10.1016/j.neuron.2009.09.020.

1083 Sanchez-Vives, M.V., and McCormick, D.A. (2000). Cellular and network mechanisms of rhythmic
1084 recurrent activity in neocortex. Nat. Neurosci. *3*, 1027-1034. 10.1038/79848.

1085 Saviane, C., and Silver, R.A. (2006). Fast vesicle reloading and a large pool sustain high bandwidth
1086 transmission at a central synapse. Nature 439, 983-987. 10.1038/nature04509.

1087 Schikorski T, Stevens CF. 1997. Quantitative ultrastructural analysis of hippocampal excitatory synapses. J
1088 Neurosci 17:5858-5867.

1089 Schikorski, T., and Stevens, C.F. (2001). Morphological correlates of functionally defined synaptic vesicle
1090 populations. Nat. Neurosci. 4, 391-395. 10.1038/86042.

1091 Schikorski, T. (2014). Readily releasable vesicles recycle at the active zone of hippocampal synapses. Proc.
1092 Natl. Acad. Sci. USA 111, 5415-5420. 10.1073/pnas.1321541111.

1093 Schindelin, J., Arganda-Carreras, I., Frise, E., Kaynig, V., Longair, M., Pietzsch, T., Preibisch, S., Rueden,
1094 C., Saalfeld, S., Schmid, B., et al. (2012). Fiji: an open-source platform for biological-image analysis. Na.t
1095 Methods 9, 676-682. 10.1038/nmeth.2019.

1096 Schmuhl-Giesen, S., Rollenhagen, A., Walkenfort, B., Yakoubi, R., Sätzler, K., Miller, D., von Lehe, M.,
1097 Hasenberg, M., and Lübke, J.H.R. (2022). Sublamina-Specific Dynamics and Ultrastructural Heterogeneity
1098 of Layer 6 Excitatory Synaptic Boutons in the Adult Human Temporal Lobe Neocortex. Cereb. Cortex 32,
1099 1840-1865. 10.1093/cercor/bhab315.

1100 Schneider, C.A., Rasband, W.S., and Eliceiri, K.W. (2012). NIH Image to ImageJ: 25 years of image
1101 analysis. Nat. Methods 9, 671-675. 10.1038/nmeth.2089.

1102 Schuman, B., Machold, R.P., Hashikawa, Y., Fuzik, J., Fishell, G.J., and Rudy, B. (2019). Four Unique
1103 Interneuron Populations Reside in Neocortical Layer 1. J. Neurosci. 39, 125-139.
1104 10.1523/JNEUROSCI.1613-18.2018.

1105 Schuman, B., Dellal, S., Pronneke, A., Machold, R., and Rudy, B. (2021). Neocortical Layer 1: An Elegant
1106 Solution to Top-Down and Bottom-Up Integration. Annu. Rev. Neurosci. 44, 221-252. 10.1146/annurev-
1107 neuro-100520-012117.

1108 Seeman, S.C., Campagnola, L., Davoudian, P.A., Hoggarth, A., Hage, T.A., Bosma-Moody, A., Baker,
1109 C.A., Lee, J.H., Mihalas, S., Teeter, C., et al. (2018). Sparse recurrent excitatory connectivity in the
1110 microcircuit of the adult mouse and human cortex. Elife 7. 10.7554/eLife.37349.

1111 Shapira M, Zhai RG, Dresbach T, Bresler T, Torres VI, Gundelfinger ED, Ziv NE, Garner CC. 2003. Unitary
1112 assembly of presynaptic active zones from Piccolo-Bassoon transport vesicles. Neuron 38:237-252.

1113 Shapson-Coe A, Januszewski M, Berger DR, Pope A, Wu Y, Blakely T, Schalek RL, Li PH, Wang S,
1114 Maitin-Shepard J, Karlupia N, Dorkenwald S, Sjostedt E, Leavitt L, Lee D, Troidl J, Collman F, Bailey L,
1115 Fitzmaurice A, Kar R, Field B, Wu H, Wagner-Carena J, Aley D, Lau J, Lin Z, Wei D, Pfister H, Peleg A,
1116 Jain V, Lichtman JW. 2024. A petavoxel fragment of human cerebral cortex reconstructed at nanoscale
1117 resolution. Science 384:eadk4858.

1118 Silver, R.A., Lübke, J., Sakmann, B., and Feldmeyer, D. (2003). High-probability uniquantal transmission
1119 at excitatory synapses in barrel cortex. Science 302, 1981-1984. 10.1126/science.1087160.

1120 Smith, H.L., Bourne, J.N., Cao, G., Chirillo, M.A., Ostroff, L.E., Watson, D.J., and Harris, K.M. (2016).
1121 Mitochondrial support of persistent presynaptic vesicle mobilization with age-dependent synaptic growth
1122 after LTP. Elife 5. 10.7554/eLife.15275.

1123 Sorra KE, Mishra A, Kirov SA, Harris KM. 2006. Dense core vesicles resemble active-zone transport
1124 vesicles and are diminished following synaptogenesis in mature hippocampal slices. Neuroscience
1125 141:2097-2106.

1126 Südhof, T.C. (2002). Synaptotagmins: why so many? J. Biol. Chem. 277, 7629-7632.
1127 10.1074/jbc.R100052200.

1128 Südhof, T.C. (2012). The presynaptic active zone. Neuron 75, 11-25. 10.1016/j.neuron.2012.06.012.

1129 Tai, X.Y., Bernhardt, B., Thom, M., Thompson, P., Baxendale, S., Koepp, M., and Bernasconi, N. (2018).
1130 Review: Neurodegenerative processes in temporal lobe epilepsy with hippocampal sclerosis: Clinical,
1131 pathological and neuroimaging evidence. Neuropathol. Appl. Neurobiol. 44, 70-90. 10.1111/nan.12458.

1132 Tang, Y., Nyengaard, J.R., De Groot, D.M., and Gundersen, H.J. (2001). Total regional and global number
1133 of synapses in the human brain neocortex. Synapse 41, 258-273. 10.1002/syn.1083.

1134 Testa-Silva, G., Verhoog, M.B., Linaro, D., de Kock, C.P., Baayen, J.C., Meredith, R.M., De Zeeuw, C.I.,
1135 Giugliano, M., and Mansvelder, H.D. (2014). High bandwidth synaptic communication and frequency
1136 tracking in human neocortex. PLoS Biol 12, e1002007. 10.1371/journal.pbio.1002007.

1137 Vaden, J.H., Banumurthy, G., Gusarevich, E.S., Overstreet-Wadiche, L., and Wadiche, J.I. (2019). The
1138 readily-releasable pool dynamically regulates multivesicular release. Elife 8. 10.7554/eLife.47434.

1139 Ventura, R., Harris, K.M. (1999), Three-dimensional relationships between hippocampal synapses and
1140 astrocytes. J. Neurosci. 19, 6897-6906.

1141 Verhoog, M.B., Obermayer, J., Kortleven, C.A., Wilbers, R., Wester, J., Baayen, J.C., De Kock, C.P.J.,
1142 Meredith, R.M., et al. (2016), Layer-specific cholinergic control of human and mouse cortical synaptic
1143 plasticity. Nat. Commun. 7, 12826. 10.1038/ncomms12826.

1144 Verstreken, P., Ly, C.V., Venken, K.J., Koh, T.W., Zhou, Y., and Bellen, H.J. (2005). Synaptic
1145 mitochondria are critical for mobilization of reserve pool vesicles at Drosophila neuromuscular junctions.
1146 Neuron 47, 365-378. 10.1016/j.neuron.2005.06.018.

1147 von Gersdorff, H., and Borst, J.G. (2002). Short-term plasticity at the calyx of Held. Nat. Rev. Neurosci. 3,
1148 53-64. 10.1038/nrn705.

1149 Watanabe, S., Trimbuch, T., Camacho-Perez, M., Rost, B.R., Brokowski, B., Sohl-Kielczynski, B., Felies,
1150 A., Davis, M.W., Rosenmund, C., and Jorgensen, E.M. (2014). Clathrin regenerates synaptic vesicles from
1151 endosomes. Nature 515, 228-233. 10.1038/nature13846.

1152 Wittner, L., Magloczky, Z., Borhegyi, Z., Halasz, P., Toth, S., Eross, L., Szabo, Z., Freund, T.F. (2001),
1153 Preservation of perisomatic inhibitory input of granule cells in the epileptic human dentate gyrus.
1154 Neuroscience 108, 587-600.

1155 Xu, N.L., Harnett, M.T., Williams, S.R., Huber, D., O'Connor, D.H., Svoboda, K., and Magee, J.C. (2012).
1156 Nonlinear dendritic integration of sensory and motor input during an active sensing task. Nature 492, 247-
1157 251. 10.1038/nature11601.

1158 Xu-Friedman, M.A., and Regehr, W.G. (2003). Ultrastructural contributions to desensitization at cerebellar
1159 mossy fiber to granule cell synapses. J. Neurosci. 23, 2182-2192. 10.1523/JNEUROSCI.23-06-02182.2003.
1160 10.1371/journal.pone.0025122.

1161 Yakoubi, R. (2023) Synaptic organization of layer 4 and layer 5 in the adult human temporal lobe neocortex:
1162 a quantitative fine-scale electron microscopic study. PhD Thesis RWTH Aachen; DOI: 10.18154/RWTH-
1163 2023-07942.

1164 Yakoubi, R., Rollenhagen, A., von Lehe, M., Shao, Y., Sätzler, K., and Lübke, J.H.R. (2019a). Quantitative
1165 Three-Dimensional Reconstructions of Excitatory Synaptic Boutons in Layer 5 of the Adult Human
1166 Temporal Lobe Neocortex: A Fine-Scale Electron Microscopic Analysis. Cereb. Cortex 29, 2797-2814.
1167 10.1093/cercor/bhy146.

1168 Yakoubi, R., Rollenhagen, A., von Lehe, M., Miller, D., Walkenfort, B., Hasenberg, M., Sätzler, K., and
1169 Lübke, J.H. (2019b). Ultrastructural heterogeneity of layer 4 excitatory synaptic boutons in the adult human
1170 temporal lobe neocortex. Elife 8. 10.7554/eLife.48373.

1171 Zagha, E. (2020). Shaping the Cortical Landscape: Functions and Mechanisms of Top-Down Cortical
1172 Feedback Pathways. Front. Syst. Neurosci. 14, 33. 10.3389/fnsys.2020.00033.

1173 Zhai RG, Vardinon-Friedman H, Cases-Langhoff C, Becker B, Gundelfinger ED, Ziv NE, Garner CC. 2001.
1174 Assembling the presynaptic active zone: a characterization of an active one precursor vesicle. Neuron
1175 29:131-143.

1176 Zhao, S., Studer, D., Chai, X., Graber, W., Brose, N., Nestel, S., Young, C., Rodriguez, E.P., Sätzler, K.,
1177 and Frotscher, M. (2012a). Structural plasticity of hippocampal mossy fiber synapses as revealed by high-
1178 pressure freezing. J. Comp. Neurol. 520, 2340-2351. 10.1111/j.1528-1167.2012.03469.x.

1179 Zhao, S., Studer, D., Chai, X., Graber, W., Brose, N., Nestel, S., Young, C., Rodriguez, E.P., Sätzler, K.,
1180 and Frotscher, M. (2012b). Structural plasticity of spines at giant mossy fiber synapses. Front. Neural
1181 Circuits 6, 103. 10.3389/fncir.2012.00103.

1182 Zhou, Y.D., and Fuster, J.M. (1996). Mnemonic neuronal activity in somatosensory cortex. Proc. Natl.
1183 Acad. Sci. USA 93, 10533-10537. 10.1073/pnas.93.19.10533.

1184

1185

1186 **Authors contributions**

1187 Conceptualization, J.H.R.L. and A.R.; Methodology, J.H.R.L., A.R. and A.S.D.; Investigation, J.H.R.L.,
1188 A.R. and A.S.D.; Writing – Original Draft, J.H.R.L., A.R. and A.S.D.; Writing – Review & Editing,
1189 J.H.R.L., A.R. and A.S.D.; Funding Acquisition, J.H.R.L. Resources, J.H.R.L.; Supervision, J.H.R.L. and
1190 A.R.

1191

1192 **Declaration of interests**

1193 The authors disclose any financial or other interests related to the submitted work that could affect, or have
1194 the perception of affecting, the author's objectivity, or could influence, or have the perception of influencing,
1195 the content of the article.

1196

1197 **Figures and legends**

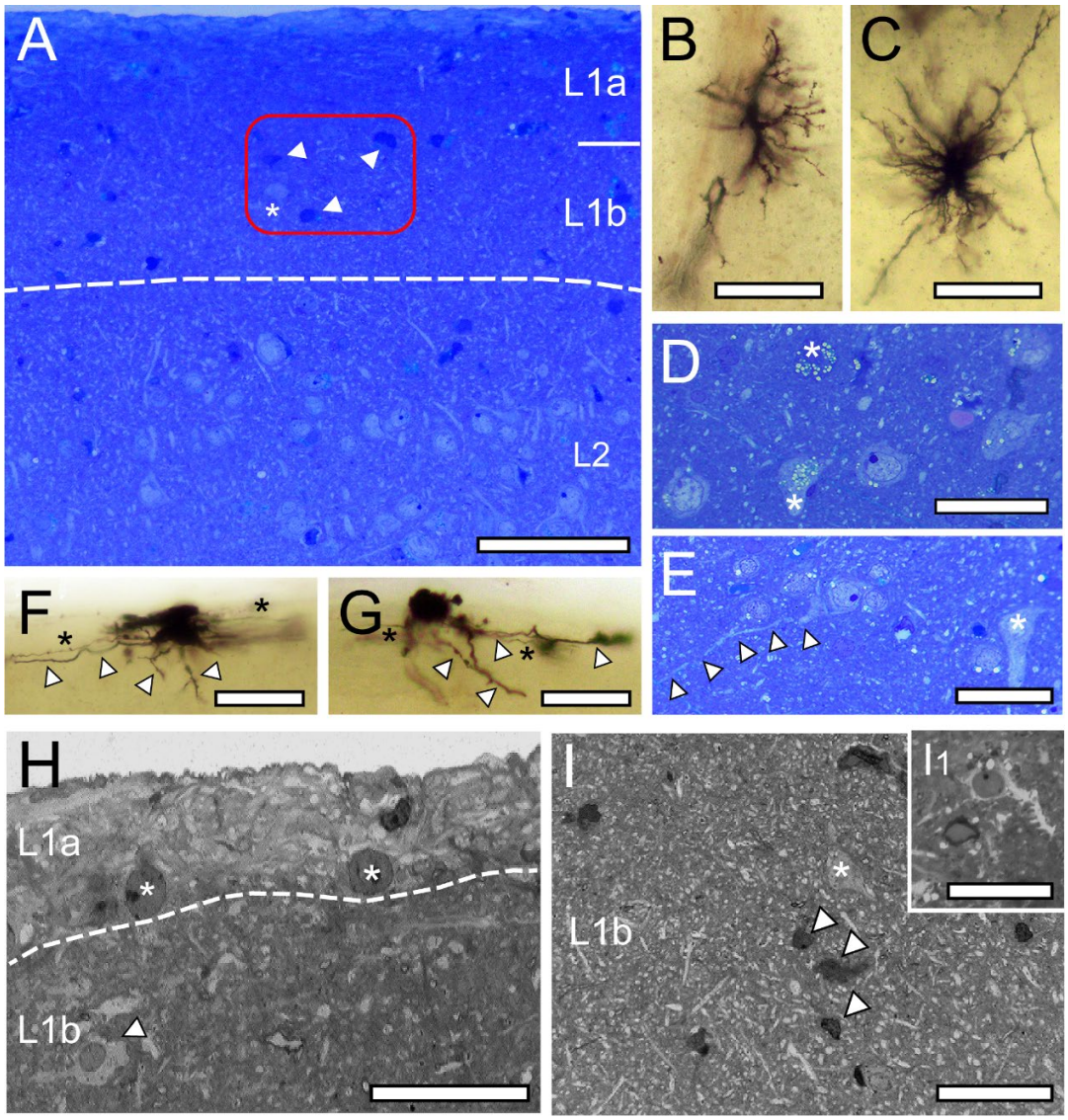

1198

1199 **Figure 1: L1 and L2 in the human TLN as revealed in methylene-blue stained semithin sections, Golgi-**
1200 **impregnation and low power EM.**
1201 **A,** Methylene-blue stained semithin section of L1a, L1b, and L2. The cell sparse zone contains degenerating
1202 neurons (dark appearance, arrowheads in the framed area) and a cell body (asterisk in the framed area). Note
1203 the sudden increase in the density of neurons at the L1b/L2 border. Scale bar 500 µm. **B, C,** Golgi-
1204 impregnated radial astrocytes in L1a (B) and L1b (C). Scale bars 50 µm. **D,** Group of neurons in L1b
1205 containing lipofuscin granules of various shape and size (asterisks) most prominent in two of the neurons.
1206 Scale bar 50 µm. **E,** Putative CR-cell identifiable by its long horizontally oriented dendrite (marked by
1207 arrowheads) and an inverted putative GABAergic interneuron (asterisk) in L1b. Scale bar 50 µm. **F, G,**
1208 Golgi-impregnated CR-Cells in L1a with the characteristic horizontal orientation of dendrites (arrowheads)
1209 and axons (asterisks). Scale bars 50 µm. **H,** EM micrograph of L1a underneath the pial surface containing
1210 two putative CR-cells (asterisks). Note the abrupt transition (indicated by the dashed line) to the neuropil of
1211 L1b, and a reactive microglial cell (arrowhead), and dendrites and synapses. Scale bar 25 µm**. I,** EM
1212 micrograph of L1b containing thousands of dendritic profiles, a putative GABAergic interneuron (asterisk)
1213 but also degenerating neurons (arrowheads) and a reactive microglia (I1) Scale bar 50 µm**.**
1214

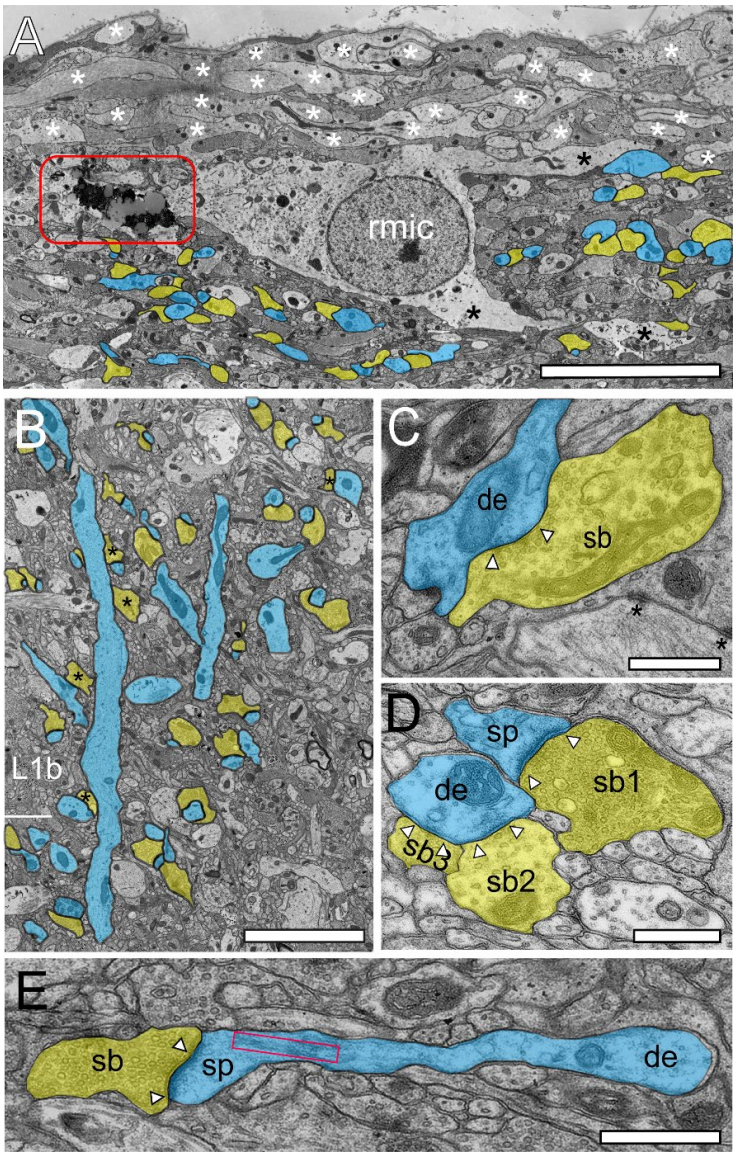

Figure 2: Structural and synaptic organization of L1 in the human TLN as revealed by EM.
A, Superficial part of L1a composed of a dense network of fine astrocytic processes (asterisks). In the reactive microglial cell (rmic) so-called lipofuscin granules (framed area) were observed. Below the astrocytic network synaptic complexes gradually increased (highlighted in blue for target structures, yellow for SBs). Scale bar 10 µm. **B,** Two apical dendrites (blue) traversing L2 with beginning terminal tuft dendrites in L2 and L1 contacted by SBs (transparent yellow); some of which are putatively GABAergic terminating on the dendritic shaft (asterisks). Scale bar 2.5 µm. **C,** Large GABAergic SB (sb, transparent yellow) identifiable by the small-sized ovoid SVs and the less prominent PSD (arrowheads) synapsing on a dendritic shaft (de, transparent blue) in L1b. **D,** Three SBs in L1a (sb1-sb3, transparent yellow) located on a dendritic spine (sp, transparent blue) and a neighboring dendritic shaft (sh, transparent blue). Note that sb1 is excitatory as indicated by the larger round SVs with a prominent AZ whereas sb2 and sb3 are putative inhibitory terminals identified by smaller ovoid SVs and the lack of a prominent PSD. **E,** Elongated spine (sp) emerging from a small caliber dendrite (de, transparent blue) receiving input from a small-sized SB (sb, transparent yellow). Note the large, elongated spine apparatus (framed area). Scale bar in C-E 0.5 µm. In graphs C-E AZs are marked by arrowheads.

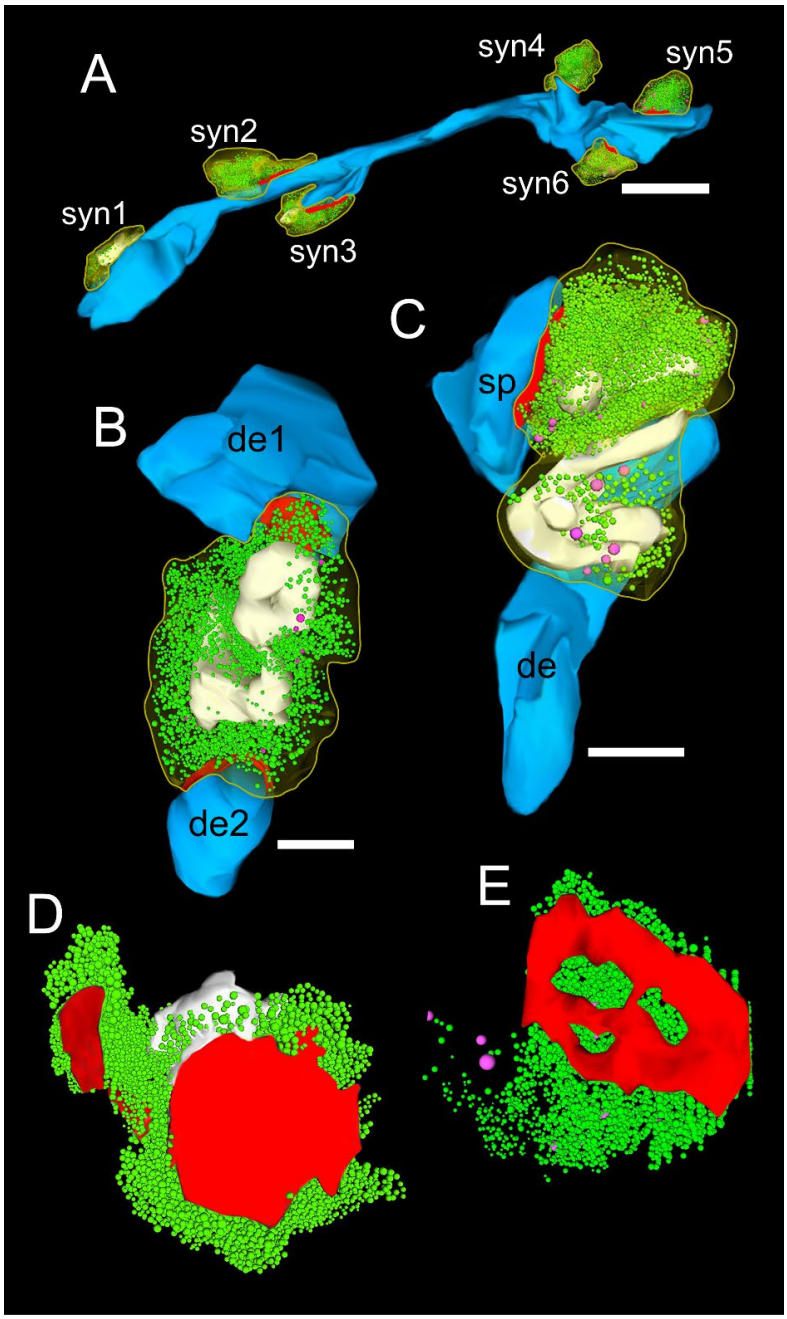

Figure 3: 3D-volume reconstructions of SBs and vesicle pools in L1a and L1b of the human TLN. **A-C,** Here, all SBs are outlined by a yellow contour. Subelements: PreAZs (red), SVs (green), DCVs (magenta), mitochondria (white). The postsynaptic target structures are given in blue **A,** Six SBs (sb1-sb6) terminating at different locations on a dendritic segment in L1b, two of which (syn3 and syn4) were located on spines, the remaining on the dendritic shaft. Scale bar 1 µm. **B,** Large SB terminating on two dendritic segments of different shape and size (de1, de2) in L1a. **C,** SB synapsing on a dendrite (de) and spine (sp) in L1b containing several mitochondria associated with the pool of SVs. **D, E,** 3D-volume reconstructions of the total pools of SVs (green dots). Note the different shape and size of the PreAZs (red) with either a non-perforated macular (D) or perforated (E) appearance and the comparably large total pool size. Note the large DCVs intermingled with the pool of SVs.

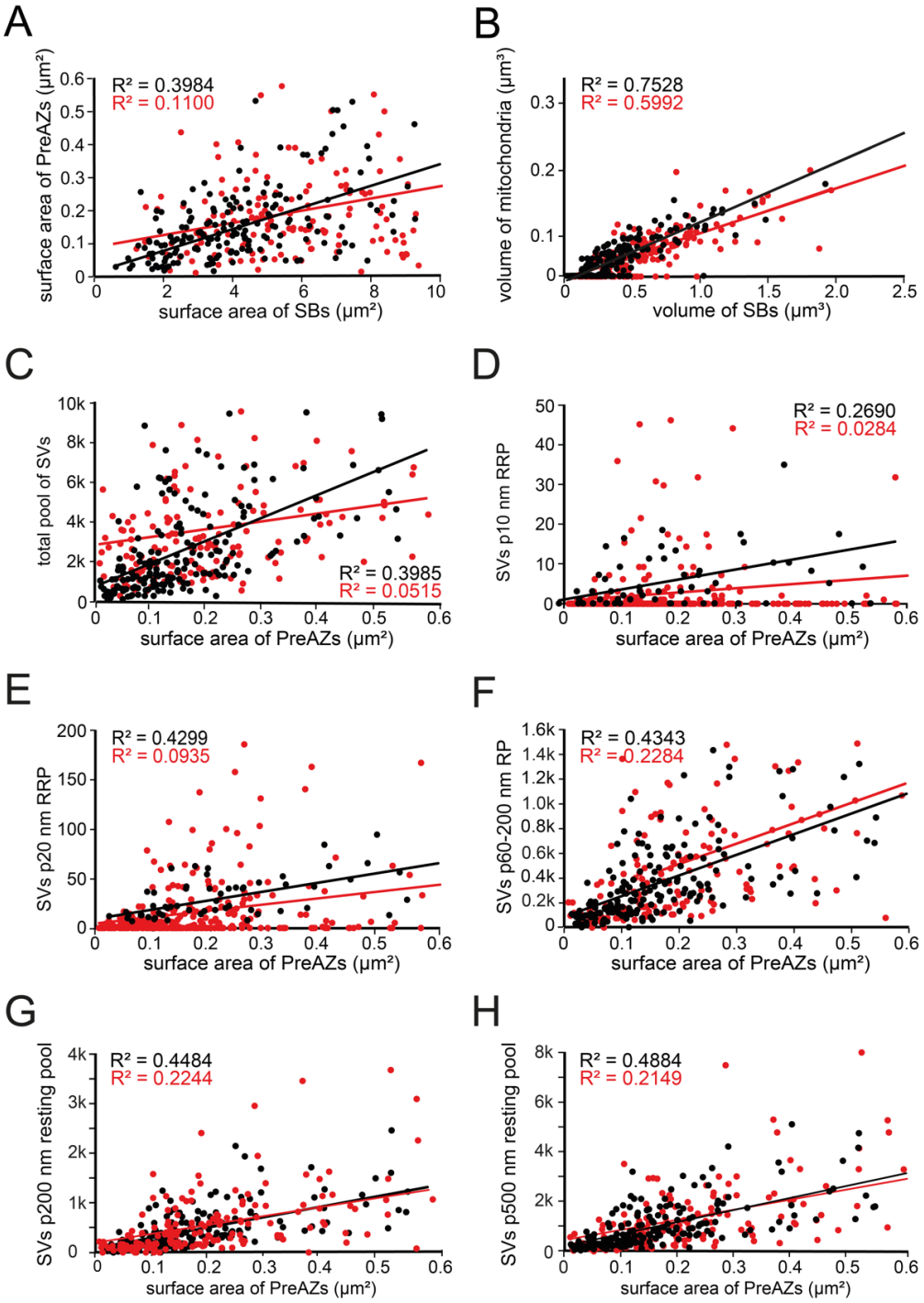

Figure 4: Correlation plots for structural and synaptic parameters characterizing L1 SBs. Correlation plots showing the strength of correlations between structural and synaptic parameters (Source Data 02). Correlations dots and regression lines for L1a are given in black and that for L1b in red. **A,** Surface area of SBs vs. surface area of PreAZs; **B,** Volume of SBs vs. volume of mitochondria; **C,** Surface area of PreAZs vs. total pool of SVs; **D,** Surface area of PreAZs vs. p10 nm RRP; **E,** Surface area of PreAZs vs. p20 nm RRP; **F,** Surface area of PreAZs vs. p60-p200 nm RP; **G,** Surface area of PreAZs vs. p200 nm resting pool; **H,** Surface area of PreAZs vs. p500 nm resting pool.

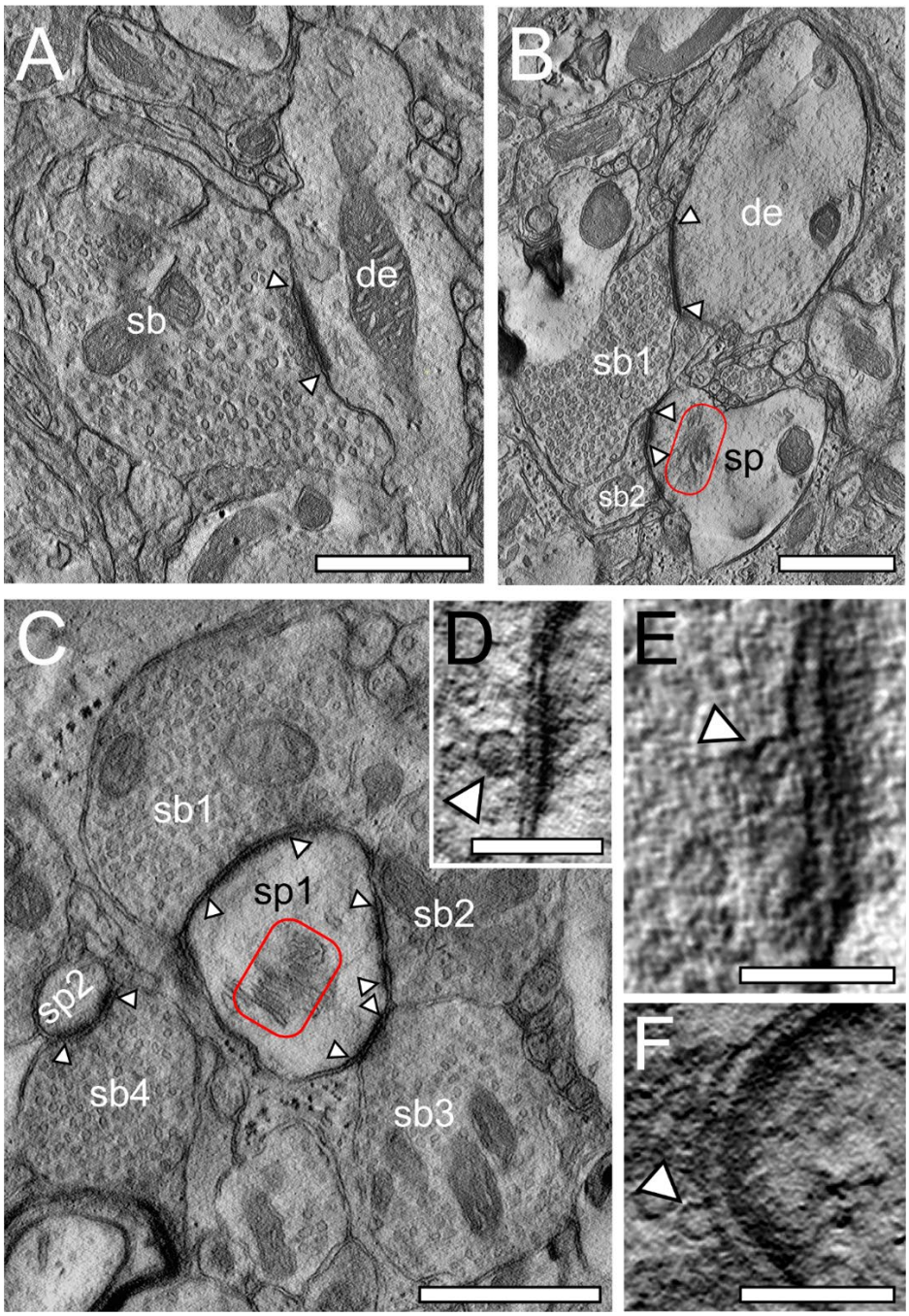

Figure 5: TEM tomography of SBs in L1a and L1b in the human TLN.
A, Large SB (sb) terminating with a single AZ (arrowheads) on a terminal tuft dendritic shaft (de) in L1a. **B,** Two adjacent SBs synapsing either (sb1) on a thick dendritic segment (de) or (sb2) on a stubby spine (sp) with a prominent spine apparatus (framed area) in L1b. Scale bars 1 µm. **C,** Large mushroom (sp1) and a small spine head (sp2) receiving input from three SBs (sb1, sb2, sb3) and a single SB (sb4) in L1b. Note the large AZs (arrowheads) and the prominent spine apparatus (red framed area) in the mushroom spine. Scale bar 0.5 µm. **D, E, F,** High-power images of 'docked' SVs (arrowheads) taken from a tilt-series through an individual PreAZ at a L1a spine SB. Note the so-called omega-shaped bodies in (E, F) pointing to the already opening and release of glutamate quanta. Scale bars 0.1 µm.

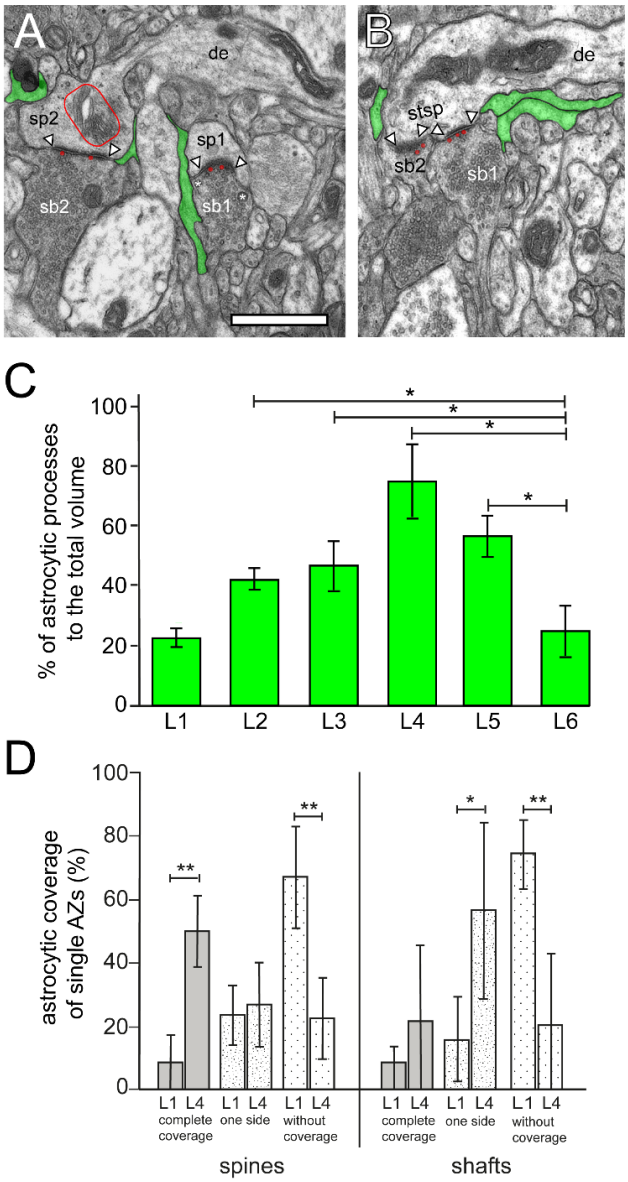

Figure 6: Astrocytic coverage of synaptic complexes in the human TLN.
A, EM micrograph of two adjacent SBs (sb1, sb2) terminating on two spines (sp1, sp2) in L1a. Sp2 contained a prominent spine apparatus (framed area), sb1 two DCVs (asterisks). Note that both synaptic complexes were only partially ensheathed by fine astrocytic processes (transparent green) reaching the AZs only on one side. In both synaptic complexes two 'docked' SVs (transparent red) at the PreAZs were found. Scale 0.25 µm. **B,** Stubby spine (stsp) receiving two SBs (sb1, sb2) in L1b. Here, fine astrocytic processes (transparent green) were found close to the two synaptic complexes but never reached the synaptic cleft. Note also the 'docked' SVs (transparent red) pointing to multivesicular release. In both images the AZs are marked by arrowheads. Scale bar 0.25 µm. **C,** Bar histogram showing the percentage (mean ± SD) of the volumetric fraction of astrocytic processes to the total volume in L1 to L6 (Source Data 04, sheet 01). Values for L4-L6 are taken from Schmuhl-Giesen et al. 2022. **D,** Bar histogram showing the percentage (mean ± SD) of AZs covered by fine astrocytic processes, either on both sides, on one side or without any coverage, subdivided by their location on dendritic spines or shafts in L1 and L4 (Source Data 04, sheet 02). The horizontal bars in C and D indicate significant differences *$p < 0.05$; **$p < 0.01$.

Table 1: Comparative quantitative analysis of various structural and synaptic parameters in L1 of the human TLN.

	Layer	Mean ± SD	Median	IQR	CV	Variance	Skewness
		Synaptic boutons					
Surface area (µm²)	L1	5.48 ± 1.40	5.75	2.20	0.26	1.96	0.21
	L1a	4.58 ± 1.13	4.27	2.20	0.25	1.28	1.13
	L1b	6.39 ± 1.08	5.87	1.97	0.17	1.17	1.66
Volume (µm³)	L1	0.50 ± 0.19	0.38	0.33	0.39	0.04	0.13
	L1a	0.41 ± 0.21	0.49	0.41	0.50	0.04	0.64
	L1b	0.58 ± 0.17	0.48	0.31	0.30	0.03	1.71
		Active zones					
PreAZ surface area (µm²)	L1	0.20 ± 0.06	0.22	0.08	0.30	0.01	-1.53
	L1a	0.18 ± 0.08	0.22	0.14	0.43	0.00	-1.70
	L1b	0.22 ± 0.04	0.22	0.08	0.18	0.00	0.00
PSD surface area (µm²)	L1	0.22 ± 0.07	0.23	0.12	0.32	0.00	-0.91
	L1a	0.21 ± 0.10	0.23	0.19	0.47	0.01	-1.02
	L1b	0.22 ± 0.05	0.22	0.09	0.20	0.00	0.33
Cleft width (nm)	L1	L: 21.75 ± 2.72 C: 29.63 ± 2.36	L: 22.20 C: 29.73	L: 2.88 C: 3.19	L: 0.13 C: 0.08	L: 7.40 C: 5.56	L: -1.03 C: -0.96
	L1a	L: 20.17 ± 2.85 C: 29.06 ± 3.48	L: 21.44 C: 29.17	L: 5.25 C: 6.95	L: 0.14 C: 0.12	L: 8.10 C: 12.08	L: -1.61 C: -0.14
	L1b	L: 23.34 ± 1.70 C: 30.19 ± 0.92	L: 22,49 C: 30.19	L: 3.06 C: 1.84	L: 0.07 C: 0.03	L: 2,88 C: 0.85	L: 1.69 C: 0.00
		Mitochondria					
Volume (µm³)	L1	0.04 ± 0.02	0.04	0.03	0.35	0.00	-0.31
	L1a	0.04 ± 0.02	0.04	0.04	0.50	0.00	0.00
	L1b	0.05 ± 0.01	0.04	0.02	0.25	0.00	1.73
% to the total volume	L1	7.21 ± 1.10	7.56	1.81	0.15	1.21	-1.13
	L1a	7.18 ± 1.60	8.06	2.81	0.22	2.56	-1.73
	L1b	7.23 ± 0.68	7.17	1.35	0.09	0.46	0.42
		Synaptic vesicles					
Total number of SVs	L1	3430.97 ± 1773.77	3675.96	3386.86	0.52	3146276.00	-0.31
	L1a	2958.62 ± 1940.51	2980.76	3880.83	0.66	3765578.00	-0.05
	L1b	3903.32 ± 1852.23	4371.16	3614.75	0.47	3430758.00	-1.06
Volume (µm³)	L1	0.03 ± 0.02	0.03	0.03	0.60	0.00	0.94
	L1a	0.02 ± 0.01	0.02	0.02	0.50	0.00	0.00
	L1b	0.04 ± 0.02	0.04	0.04	0.50	0.00	0.00
Vesicle diameter (nm)	L1	25.03 ± 5.67	26.36	10.38	0.23	32.13	-0.31
	L1a	23.33 ± 5.27	25.88	9.56	0.23	27.74	-1.67
	L1b	26.73 ± 6.63	28.25	12.99	0.25	43.93	-0.98
	L1 *	30.29 ± 4.67	31.10	3.21	0.15	21.77	-2.60
	L1a*	28.11 ± 6.10	30.15	3.91	0.22	37.17	-2.04
	L1b*	31.88 ± 2.36	31.62	3.27	0.07	5.56	0.04
		Pool sizes of SVs					
Putative RRP p10 nm from the PreAZ	L1	3.60 ± 4.24	2.10	6.98	1.18	17.99	1.17
	L1a	5.90 ± 5.05	6.11	10.10	0.86	25.53	-0.18
	L1b	1.29 ± 1.87	0.41	3.41	1.44	3.49	1.65
Putative RRP p20 nm from the PreAZ	L1	19.05 ± 17.23	17.17	29.37	0.90	296.86	0.67
	L1a	25.04 ± 21.09	24.82	42.18	0.84	444.82	0.05
	L1b	13.07 ± 13.78	9.52	26.86	1.05	189.80	1.08
Putative RP 60-200 nm from the PreAZ	L1	463.00 ± 283.82	512.65	554.39	0.61	80553.57	-0.19
	L1a	390.12 ± 286.89	335.05	565.79	0.74	82304.11	0.83
	L1b	535.88 ± 321.16	690.25	584.03	0.60	103145.30	-1.66
Putative resting pool > 200 nm from the PreAZ	L1	2896.50 ± 1435.93	3120.39	2698.41	0.50	2061880.00	-0.38
	L1a	2515.02 ± 1588.99	2662.80	3167.65	0.63	2524880.00	-0.41
	L1b	3277.97 ± 1480.96	3577.98	2915.99	0.45	2193254.00	-0.87

Summary of different structural parameter measurements (bold) from the detailed 3D-volume reconstructions of SBs in L1, separated for sublaminae. Values are presented as mean, SD, median, IQR, CV, skewness, and variance for each parameter for all patients studied. #: Values with skewness > 3 indicate a non-normal distribution. Abbreviations: IQR: Interquartile Range; CV: coefficient of variation; L: lateral; and C: central (Source Data 02; Source Data 03). *Values collected from TEM tomography.

Table 2: 'Docked SVs' in L1a and L1b of the human TLN.

	Layer	Mean ± SD	Median	IQR	CV	Skewness	Variance
Number of docked vesicles	**L1** (n=360 SVs)	3.56 ± 1.36	4.00	3.00	0.38	-0.07	1.85
	L1a	3.71 ± 1.38	4.00	3.00	0.37	-0.16	1.89
	SBs on dendritic shafts (n=91 SVs)	3.64 ± 1.47	4.00	3.00	0.40	-0.08	2.16
	SBs on dendritic spines (n=98 SVs)	3.77 ± 1.31	4.00	2.00	0.35	-0.24	1.70
	L1b	3.42 ± 1.34	3.00	3.00	0.39	0.02	1.80
	SBs on dendritic shafts (n=87 SVs)	3.48 ± 1.45	3.00	3.00	0.42	0.04	2.09
	SBs on dendritic spines (n=84 SVs)	3.36 ± 1.25	3.00	2.50	0.37	-0.07	1.57

Summary of the number of 'docked' SVs in L1, separately for both sublaminae as well as for the different target structures dendritic shafts vs. dendritic spines. Mean ± SD, Median, Interquartile Range (IQR), coefficient of variation (CV), Skewness, and Variance are given for each parameter in all patients studied (Source Data 03).

Table 3: Astrocytic coverage of synaptic complexes in the human TLN.

Layer / Measurement	**L1** (Mean ± SD)	**L2** (Mean ± SD)	**L3** (Mean ± SD)	**L4** (Mean ± SD)	**L5** (Mean ± SD)	**L6** (Mean ± SD)
Percentage of astrocytic processes to the total volume						
	23.23 ± 6.90	43.10 ± 3.38	48.42 ± 10.06	76.71 ± 12.94	58.13 ± 9.15	25.16 ± 9.56
Astrocytic coverage of single AZs (%)						
Spine synapses	n=254 (L1a: 128; L1b: 126)	—	—	n=93	—	—
Complete coverage	8.69 ± 9.10			50.21 ± 11.21		
One side	23.73 ± 9.29			27.26 ± 13.04		
Without coverage	67.57 ± 15.78			22.52 ± 12.77		
Shaft synapses	n=92 (L1a: 48; L1b: 44)	—	—	n=41	—	—
Complete coverage	8.54 ± 5.39			22.09 ± 24.16		
One side	16.44 ± 13.16			57.30 ± 27.80		
Without coverage	75.02 ± 10.89			20.61 ± 22.23		

Summary of astrocytic coverage of synaptic complexes in the human TLN in L1 and L4 measured with two independent experimental approaches: 1) percentage of astrocytic processes contributing to the total volume and 2) percentage of astrocytic coverage around individual AZs.

1304 **Supplemental Information**

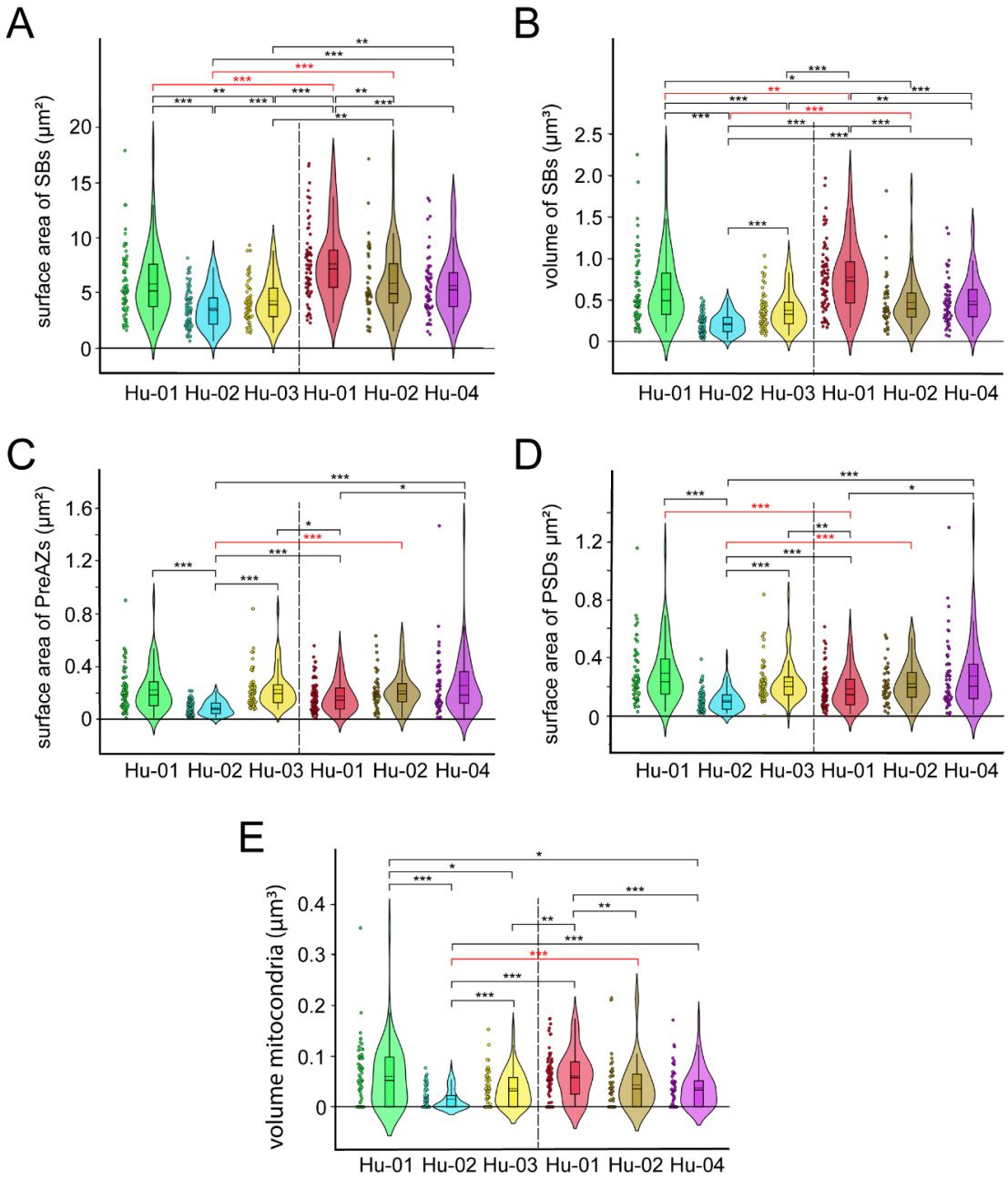

1305

1306 **Supplemental Figure 1: Box plots of various structural parameters in L1 of the human TLN**
1307 Data distributions for each patient in L1a (left side of dashed line) and L1b (right side of dashed line) are
1308 indicated by the medians (horizontal bars), IQRs (framed areas), minimum and maximum (vertical lines)
1309 for the distribution of: A, Surface area of SBs; B, Volume of SBs; C, Surface area of PreAZs; D, Surface
1310 area of PSD; E, Volume of mitochondria. Significant differences between different patients are indicated
1311 by asterisks. Note that several structural parameters are significantly different. The significant bars
1312 highlighted in red indicate significant differences between sublaminae L1a and L1b in the same patient. *:
1313 $p < 0.05$; **: $p < 0.01$; ***: $p < 0.001$ (Source Data 02). Hu_01 and Hu_02 were selected for both L1a and
1314 L1b in separate serial sections each.
1315

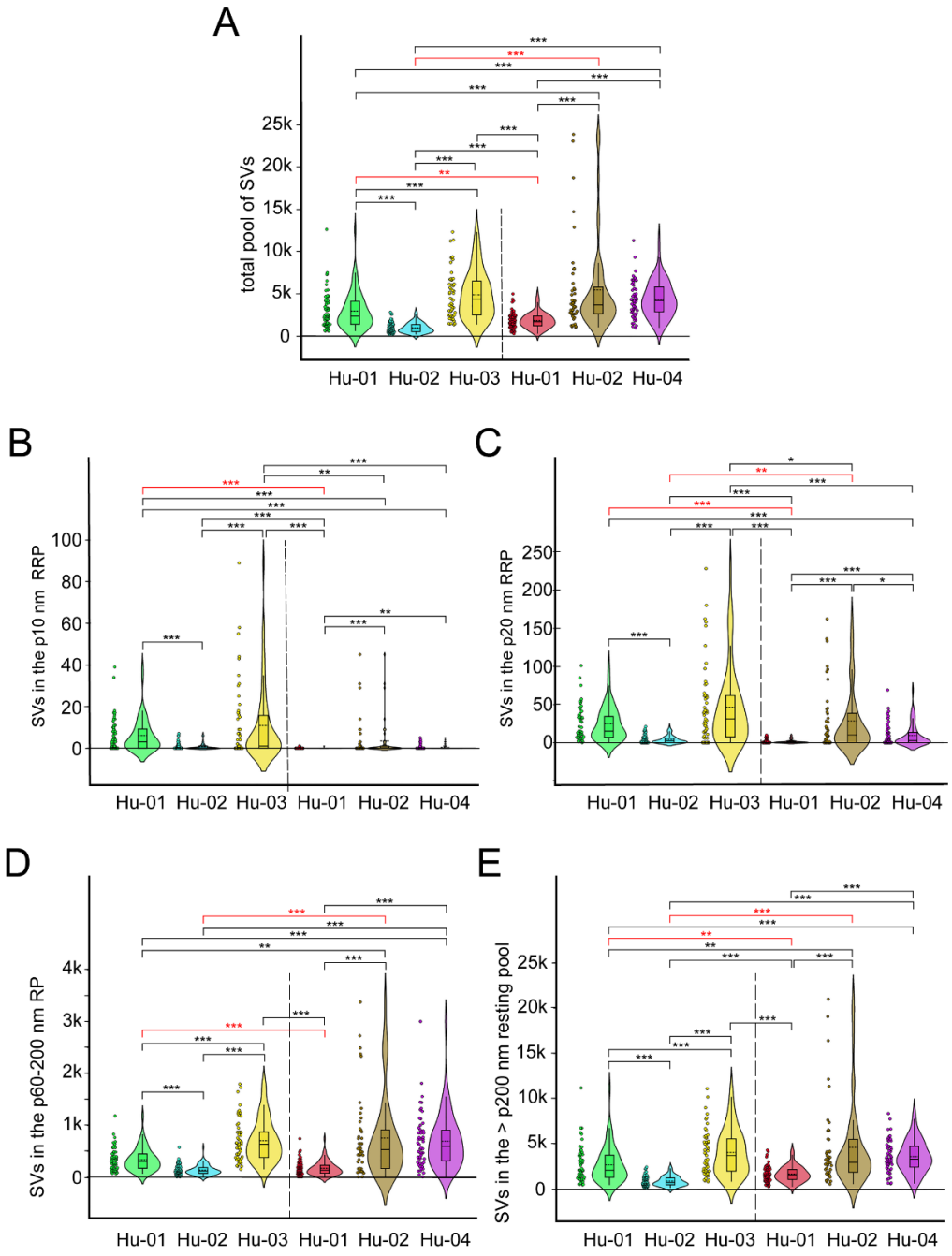

Supplemental Figure 2: Box plots of various synaptic parameters in L1 of the human TLN
Data distributions for each patient in L1a (left side of dashed line) and L1b (right side of dashed line) are indicated by the medians (horizontal bars), IQRs (framed areas), minimum and maximum (vertical lines) for the distribution of: **A,** Total pool of SVs; **B,** SVs in the p10 nm RRP; **C**, SVs in the p20 nm RRP; **D**, SVs in the p6-200 nm RP; **E**, SVs in the > p200 nm resting pool; Note that several structural parameters are not significantly different. The significant bars highlighted in red indicate significant differences between sublaminae L1a and L1b in the same patient. *: $p < 0.05$; **: $p < 0.01$; ***: $p < 0.001$ (Source Data 02). Hu_01 and Hu_02 were selected for both L1a and L1b in separate serial sections each.

1326 **Supplemental Table 1: Comparison of the synaptic density between L1a, L1b and L4 – L6 of the**
1327 **human TLN**

Cortical layers	L1a mean ± SD	L1b mean ± SD	Total L1 mean ± SD	L4 mean ± SD	L5 mean ± SD	L6 mean ± SD
Density of synaptic contacts/mm^3	$5.52*10^8$ ± $1.25*10^8$	$5.01*10^8$ ± $1.40*10^7$	$5.26*10^8$ ± $8.44*10^7$	$2.37*10^6$ ± $2.19*10^6$	$3.89*10^8$ ± $9.12*10^8$	$4.98*10^7$ ± $1.85*10^7$

1328 Values for L4–L6 are taken from: L4: Yakoubi et al. 2019b; L5: Yakoubi R., PhD Thesis 2023; L6:
1329 Schmuhl-Giesen et al. 2022.
1330
1331
1332
1333 **Supplemental Table 2: Patient's identity and medical background**

Patient's identity and medical background	Gender	Age (years)	Age at epilepsy onset (years)	Histo-Pathology	Antiepileptic drugs (pre-op)	Number of SBs recon-structed
Hu_01	♂	52	20	AHS	LEV, OXC, Perampanel	L1a: 63; L1b: 70
Hu_02	♀	27	16	Micro- and Astrogliosis	LEV, Topiramat, Zebinix	L1a: 72; L1b: 45
Hu_03	♀	65	1	Hippocampal sclerosis	LEV, LTG, Primidone	L1a: 55
Hu_04	♀	24	N/A	TLE	N/A	L1b: 56
Hu_05*	♀	36	4	GGL	LEV, LTG	
Hu_06*	♀	25	12	AHS	LTG	
Hu_07*	♀	25	23	GGL	Zebinix, LEV	
Hu_08*	♂	33	5	Gliosis	LEV, CBZ	
Hu_09*	♂	63	24	AHS	LEV, LTG, CBZ	

1334 Abbreviation: AHS: Ammon's horn sclerosis; CBZ: Carbamazepine; GGL: Ganglioglioma; LEV:
1335 Levetiracetam; LTG: Lamotrigine; OXC: Oxcarbazepin; TLE: Temporal Lope Epilepsy. *Hu_05 – Hu_09
1336 were only used to analyze the astrocytic coverage of AZs in L4.